

First use of a HyViSI H4RG for astronomical observations

Lance M. Simms^a, Donald F. Figer^b, Brandon J. Hanold^b, Daniel J. Kerr^b, D. Kirk Gilmore^a,
Steven M. Kahn^a, J. Anthony Tyson^c

^aStanford Linear Accelerator Center, Menlo Park, CA, 94025 USA;

^bRochester Imaging Detector Laboratory, Rochester, NY 14623 USA;

^cDepartment of Physics, University of California, Davis, CA 95616 USA

ABSTRACT

We present the first astronomical results from a $4K^2$ Hybrid Visible Silicon PIN array detector (HyViSI) read out with the Teledyne Scientific and Imaging SIDECAR ASIC. These results include observations of astronomical standards and photometric measurements using the 2.1m KPNO telescope. We also report results from a test program in the Rochester Imaging Detector Laboratory (RIDL), including: read noise, dark current, linearity, gain, well depth, quantum efficiency, and substrate voltage effects. Lastly, we highlight results from operation of the detector in window read out mode and discuss its potential role for focusing, image correction, and use as a telescope guide camera.

Keywords: H4RG, HyViSI Pin Array, SIDECAR ASIC

1. INTRODUCTION

The Hybrid Visible Silicon (HyViSI) H4RG is a hybrid CMOS (Complimentary Metal-Oxide-Semiconductor) $4K \times 4K$ optical imager produced by Teledyne Scientific and Imaging (TIS). It consists of an H4RG multiplexer that acts as a Readout Integrated Circuit (ROIC) and a $100 \mu m$ -thick layer of high purity bulk silicon that serves as the photo-detector. The two are sandwiched together, or *hybridized*, via indium bump bonds at the surface of each $10 \mu m \times 10 \mu m$ pixel. On the ROIC side, the pixel consists of addressing, resetting, and readout circuitry and on the silicon side the unit cell contains a photodiode that collects photocharge at the site of a p+ implant. A high voltage source is attached to the illuminated side of the silicon layer in order to fully deplete the bulk of charge carriers. This provides a large depletion region for long wavelength photons to promote electrons into the conduction band and inhibits the lateral diffusion of charge that tends to degrade the point spread function (PSF).

The hybrid CMOS architecture of the HyViSI H4RG and other hybrid CMOS sensors offers many of the advantages of conventional CMOS devices and leaves behind some of the drawbacks of CCDs and non-hybrid CMOS devices. As with most CMOS devices, operation of the H4RG sensor consumes very low power (operated at 3.3V and lower) and enables on-chip integration of analog and digital circuitry.¹ The CMOS architecture also eliminates the need to shift charge toward an output by allowing non-destructive, random access to the pixels; only one pixel-based charge-to-voltage conversion is necessary. Since any pixel can be accessed independently of the others, CMOS detectors do not suffer from charge transfer inefficiency (CTE) due to radiation damage, where a charge trap in one pixel can affect all of the ones following it in its row. The random access also allows a sub-region of the detector to be read out continuously at fast rates, allowing for photometric measurements of bright and/or rapidly-varying sources.

The $100 \mu m$ layer of silicon photodiodes atop the ROIC overcomes the problems of small fill-factor and inefficient charge collection associated with monolithic CMOS sensors.² It offers nearly 100% fill factor and when fully depleted, the layer provides good quantum efficiency from the ultraviolet to $1.15 \mu m$ at the cutoff of silicon. As in the case of fully depleted thick CCDs, this large depletion region also provides a greater interaction depth for high energy particles from cosmic rays and radioactive decay that result in wandering tracks and loss of imaging pixels.³ However, the non-destructive readout scheme implemented in CMOS devices offers a key advantage over the destructive one used in a CCD. The non-destructive reads allow up-the-ramp sampling that, in addition to lowering the read noise by sampling the voltages of each pixel multiple times during an integration, provides robust cosmic ray rejection with only one exposure. This is in contrast to CCDs, where typically two

or more exposures of the same length of time are required. The tradeoff is in the larger data volume associated with multiple up-the-ramp samples. If B_p is the number of bytes per pixel associated with the data, two CCD exposures with $X \times Y$ pixels will yield $2X * Y * B_p$ bytes while one CMOS up-the-ramp exposure with N reads will yield $N * X * Y * B_p$ bytes. Typically, 5 or more reads are required to reject cosmic rays with confidence.

The H4RG is a new device and only a small number of prototypes have been manufactured. One of them, H4RG-10-007, was purchased by the Large Synoptic Survey Telescope Corporation (LSST Corp.) and loaned to us at the Rochester Imaging Detector Laboratory for testing and characterization. The detector was read out by a TIS SIDECAR ASIC chip that provided an exceptional amount of functionality in a very small volume as well as Generation III electronics from Astronomical Research Cameras (ARC).

In the following sections of this paper, we present pixel characterization and laboratory measurements of dark current, read noise, electron conversion gain, well depth, linearity, and quantum efficiency for the HyViSI H4RG. We compare these results to those from other Si PIN devices. We then describe the process of reducing the data taken at the telescope and show the results from relative photometry of standard stars and the M13 globular cluster. Lastly, we discuss the data collected in *window mode* and use it to illustrate the potential of the H4RG as a detector for telescope focusing, image correction, and guiding.

2. LABORATORY TESTING

The goal of our lab testing program is to characterize Si PIN array technology for use in astronomical applications, with an emphasis on tests of the H4RG-10-007 device. Our testing follows a similar program used to evaluate JWST detectors.⁴ The testing yields measurements of the most relevant properties, i.e. gain, read noise, dark current, linearity, etc., over a wide range of operational variations, i.e. temperature, read mode, and post-processing electronics architecture. The testing was performed in the Rochester Imaging Detector Laboratory (RIDL) within the Center for Imaging Science at Rochester Institute of Technology. The RIDL is a new facility dedicated to the development of detector technologies for multi-disciplinary applications.

2.1 RIDL System

The RIDL system (see Figure 1) consists of software and hardware based on a system used to characterize infrared and optical detectors for space- and ground-based applications.⁵ The modular architecture of the system allows for rapid acquisition and reduction of large datasets over a broad range of experimental conditions. Minimal effort is required to change between different detectors and different types of detectors. The system can be transported for operation on a telescope.

The system includes a 16 inch diameter dewar (Universal Cryogenics, Tucson, AZ) with a 110 mm diameter CaF2 window, two cryogenic filter wheels, and a detector enclosure. The system is cooled with a two-stage cooler (CTI Model 1050, Brooks Automation, Chelmsford, MA), and the detector is thermally stabilized with a 10-channel temperature controller (Lakeshore Cryotronics, Westerville, OH). The detector enclosure provides thermal and electrical feedthroughs, an entrance window, and an otherwise light-tight cavity for the detector. The filter wheels can accommodate eight filters and/or radiation sources. We use two sets of readout electronics: 1) the Generation III electronics from Astronomical Research Cameras, Inc. (San Diego, CA), and 2) the SIDECAR ASIC from Teledyne Scientific & Imaging, LLC (Thousand Oaks, CA). We used a variety of programmable gains to obtain data and 5 us pixel time for the ARC electronics and 10 us pixel time for the SIDECAR.

2.2 Electronic Gain/Conversion Gain

There are a number of electrical gain stages in the signal path, and they collectively produce a net conversion gain, G_{net} , in units of e^-/ADU :

$$G_{net} = G_{pixel} * G_{UC} * G_{OUT} * G_{AMP} * G_{A/D} \quad (1)$$

The pixel gain, G_{pixel} (e^-/V), represents the voltage change per unit charge, also known as the inverse of the capacitance. It is linear over small signal ranges but becomes nonlinear when the pixel is near capacity. The detector readout has two source follower FETs between each pixel and the output pad. One is in each unit cell,

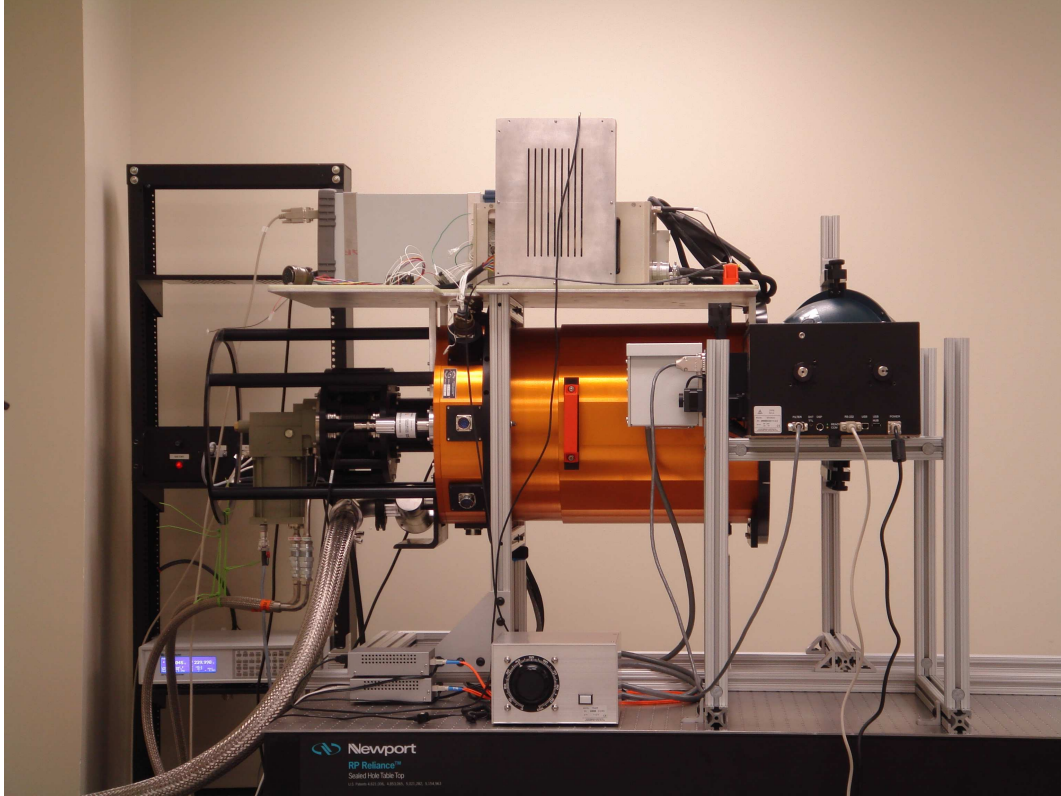


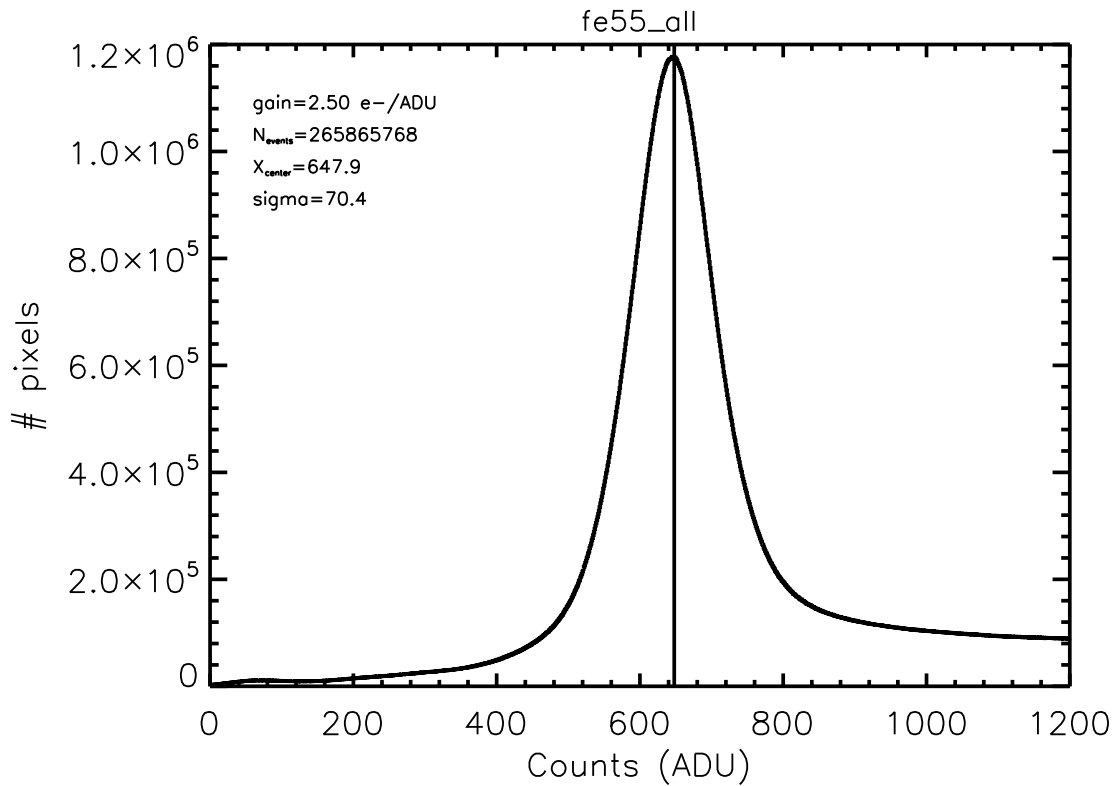
Figure 1. RIDL system. An orange dewar houses two filter wheels and a detector enclosure. A helium cryo-cooler cools the system. The picture shows an integrating sphere and monochromator near the front of the dewar. Post-processing electronics are mounted on a plate attached to the top side of the dewar. Off camera are three computers (two four-way and one eight-way CPU) with 4 GB, 12 GB, and 16 GB of RAM and 12 TB of RAID5 storage.

and it induces a gain of G_{UC} (V/V). The other, the output FET, introduces a similar gain, referred to as G_{OUT} (V/V). The processing electronics have stages to amplify the signal, G_{AMP} (V/V). Finally, $G_{A/D}$ (V/ADU), represents the conversion between volts and analog to digital units (ADUs). We have developed procedures to measure each of these gains.

First, we establish $G_{A/D}$ by dividing the range of ADUs measured as a response to a well-characterized sawtooth pattern by the voltage range of that sawtooth. This measurement is done without the amplifier gain stage in the circuit. Next, we measure G_{AMP} by repeating the sawtooth experiment with the gain stage in the circuit. We find G_{UC} by bypassing the output FET and measuring the response to a varying reset voltage programmed onto the gate of the pixel FET. Next, we repeat the reset experiment with the output FET in the circuit in order to measure G_{OUT} . Finally, G_{pixel} is inferred by inverting the equation above and using the full conversion gain from our Fe55 experiment. In this experiment, an Fe55 source is placed an inch above the detector and we operate the device in photon-counting mode. The conversion gain is simply 1620 electrons divided by the peak of the photon hit distribution. Table 1 summarizes the gain measurements for the H4RG-10-007 detector and the ARC electronics. Note that the measurements are given for two different amplifier gains. Figure 2 shows a photon counting image and histogram produced by this experiment.

Table 1. Measured gains using the ARC electronics and the H4RG-10-007 Si PIN detector

H4RG ARC SFE							
G_{AMP}	Fe55 peak	Conversion Gain	$G_{A/D}$	Unit Cell Gain	$G_{UC} * G_{OUT}$	$1/G_{pixel}$	Unit Cell Capacitance
(V/V)	(ADU)	(e^-/ADU)	($\mu V/ADU$)	($\mu V/ADU$)	(V/V)	($\mu V/e^-$)	(fF)
1.81	699.2	2.32	42.97	58.411	0.736	25.21	6.347
6.62	2590	0.63	11.08	15.292	0.725	24.45	6.544



\\howk\RAID1\H4RG-10-007\cold2\Leach\30July07_Fe55\fe55_all.ps

Figure 2. Histogram of signal generated by x-ray photons from Fe55. The photons each liberate 1620 electrons; the conversion gain $1620/647.9=2.5$ electrons/ADU.

2.3 Pixel Characterization

We have identified several different types of pixels on the H4RG that cannot be used to accurately estimate luminance. They are categorized as dead, hot, and open pixels. These pixels are masked and not used in the analysis of our observational data. All of the other pixels on the detector are of suitable quality to be used in the observational data analysis.

2.3.1 Dead Pixels

The first type of unusable pixels are dead pixels that do not integrate charge, whether exposed to light or not. Most of them are railed at the high end of the detector voltage range, suggesting they are shorted to one of the high bias voltages. These pixels are easy to detect since they do not show an increase in signal over time. In order to find them, we took differences between a read r and the zeroth read $r = 0$, in the flat field and dark images and flagged pixels that had a difference in signal, I , below a certain threshold T . i.e.

$$I(x, y, r + 1) - I(x, y, 0) < T, \quad (2)$$

for all r . T depends on the gain of the pre-amps in the SIDECAR ASIC, but is typically set at $3 \times N_r$, where N_r is the read noise of the detector at that gain.

In all, there are 6341 of these pixels on the detector, representing 0.038% of the total number of pixels. This number includes an entire row of 4096 pixels that is presumably a bad line in the ROIC.

2.3.2 Hot Pixels

The hot pixels are found by (1) looking for very high pixel signal slopes, $\Delta I/\Delta t$, and (2) looking for pixels that have a value of I greater than 75% of the full A/D range in the zeroth read. In the latter case, the dark current is so extreme that the pixel voltage reaches the upper rail almost immediately after reset, and its slope is flattened before the zeroth read. There are a total of 210,063 (1.252%) pixels that meet this criteria.

2.3.3 Open Pixels

The open pixels are pixels that have a value that falls significantly below that of their nearest neighbors in well-illuminated images. I.e.

$$I(x, y, r) \ll I(x \pm 1, y \pm 1, r). \quad (3)$$

These pixels are presumed to be open in the sense that the indium bump bond does not connect the silicon substrate to the ROIC. Their spatial distribution over the detector is not uniform over the detector, and it has been mapped to a set of suspected opens by Teledyne. There are a total of 76,959 open pixels on the detector, representing 0.459% of the total population.

Figure 3 shows isolated black squares and black squares surrounded by neighbors with enhanced signal. We associate the former with hot pixels. We have verified that their signal quickly reaches saturation such that they appear dark in a difference image. The black pixels with bright neighbors are open pixels, i.e. pixels with poor bump bond interconnects.

While the open pixels appear to be dead in the stretch shown in the figure, they do have increasing signal versus read number, but the slope does not depend on the presence of light. Their neighbors have extraordinarily large signal. In a flat field image, the cumulative augmented signal in the eight nearest neighbors to an open

Table 2. Bad pixels

Pixel Type	Number	Fraction	Characteristics
Dead	6341	0.038%	no signal accumulation
Hot	210,063	1.252%	rapid signal accumulation
Open	76,959	0.459%	nearest neighbors show rapid accumulation

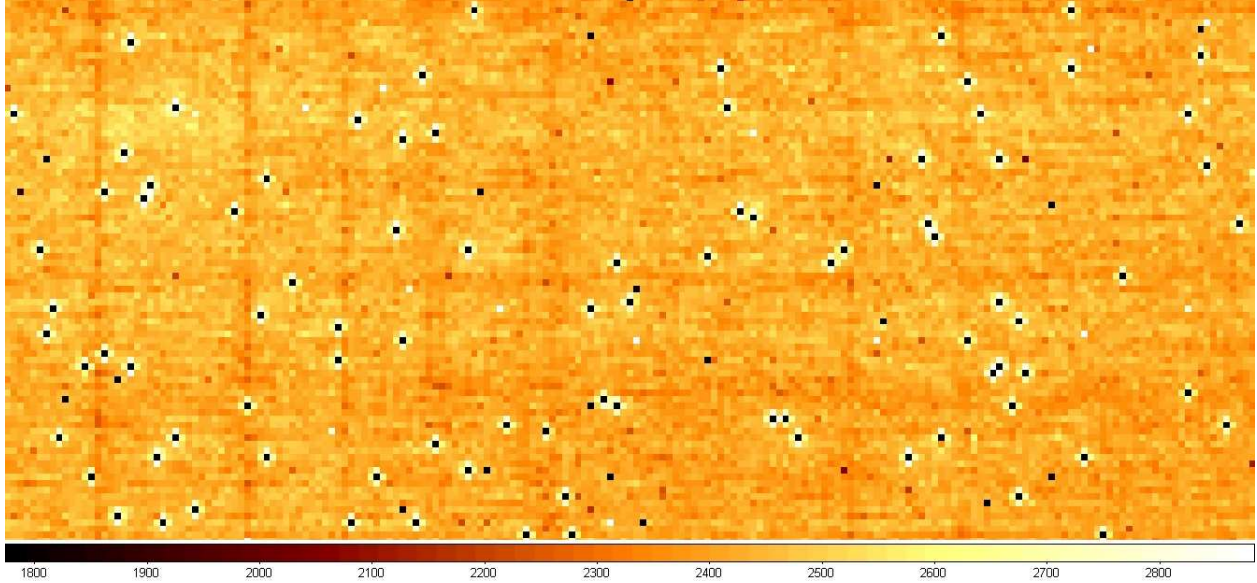


Figure 3. Difference image of portion of H4RG-10-007 array under flat field illumination at 1000 nm. Notice that there are two populations of dark pixels. One is surrounded by neighbors with normal response and another is surrounded by pixels with elevated apparent response. The former are identified as hot pixels which have a difference near zero and the latter are identified as open pixels.

pixel is 70% of the signal that should have been in the open pixel. Interestingly, 30% of the signal that should be in the open pixel is unaccounted for. Perhaps the open pixels have very high impedance connections to the readout circuit so that they integrate some charge; however, most of the charge generated in the bulk material of the pixel migrates to neighbors. (Note that by just looking at the figure, one might propose that the "open" pixels are actually very hot pixels that difference to zero in the difference image in the figure. In this case, one might suggest that the neighbors have enhanced signal because of interpixel capacitance. This cannot be true, because we have verified that the open pixels do indeed have low counts in individual reads - they are never saturated).

2.4 Reference Pixels and Channels

The H4RG ROIC contains two types of reference pixels. The first type is identical to science pixels, except the backside has been blackened to prevent light from entering the substrate. The second type consists of capacitors with a capacitance C_{pix} similar to the detector capacitance and is the same as in previous HxRG designs. In practice, we found that the two different types of reference pixels have dramatically different behavior. Figure 4 shows that the blackened type has dark current that is similar to that in nearby science pixels. On the other hand, the capacitor type does not integrate dark charge. Depending on the goal, one might choose to use either pixel type. For instance, if one wants to remove common mode interference, then the capacitor type might be the most useful. On the other hand, one could use the blackened type to remove this interference and also some portion of the dark current. For characterizing the detector technology, we found it useful to not use reference pixel subtraction. We saw no noise penalty in doing this.

2.5 Well Depth and Linearity

We measure the well depth and linearity by exposing the detector to a flat illumination source and obtaining a ramp with many reads through the saturation level. Figure 5 shows that the H4RG-10-007 detector saturates at about $55 ke^-$, and that the saturation level varies by about 2%. Figure 6 shows the saturated image; note the population of bad (open) pixels that do not respond to light. The linearity plot, in the bottom panel of Figure 5 shows the average of normalized slopes for all of the pixels on the detector at a particular ADU value. The normalization is with respect to the slope between the first and zeroth read of the ramp for each pixel. The figure

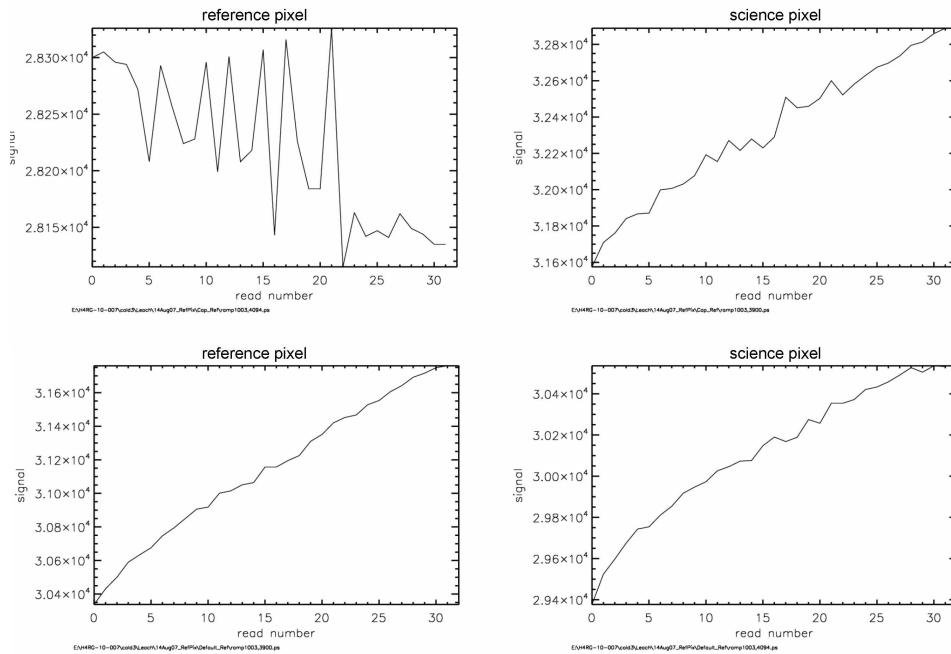


Figure 4. Behavior of reference pixels. The capacitor-type reference pixels do not integrate dark current charge (upper left) as do the science pixels (upper right). The blackened reference pixels do integrate dark current charge (lower left), similar to what is seen for a science pixel in the same image (lower right).

shows that the detector is linear to within a few percent over 90% of its well range, and that the non-linearity is well-fit by a second order polynomial, to within a few tenths of a percent over most of the well range. This non-linearity is reproducible to within a few tenths of a percent.

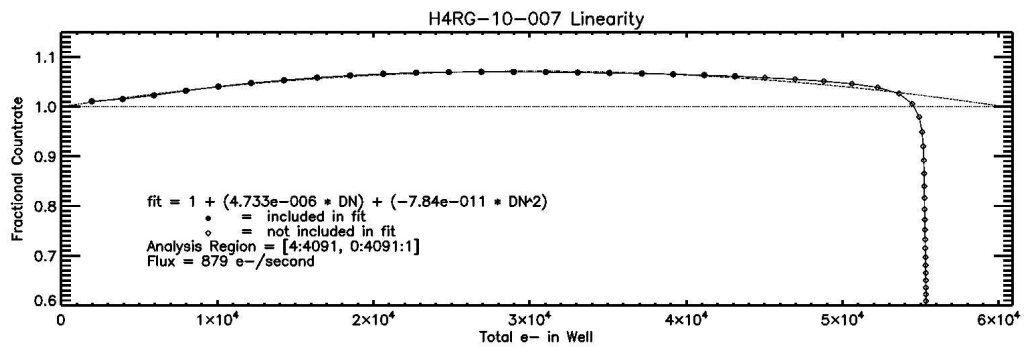
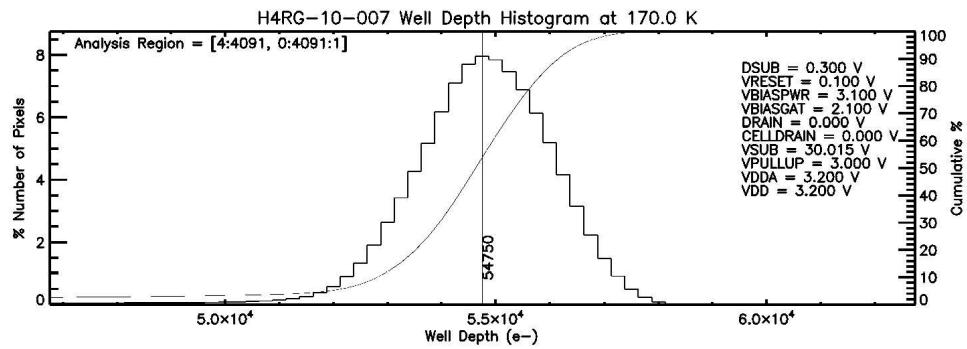


Figure 5. Histogram of well capacity (top) and linearity versus fluence (bottom).

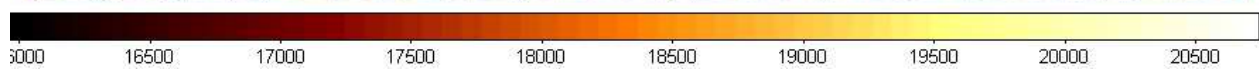
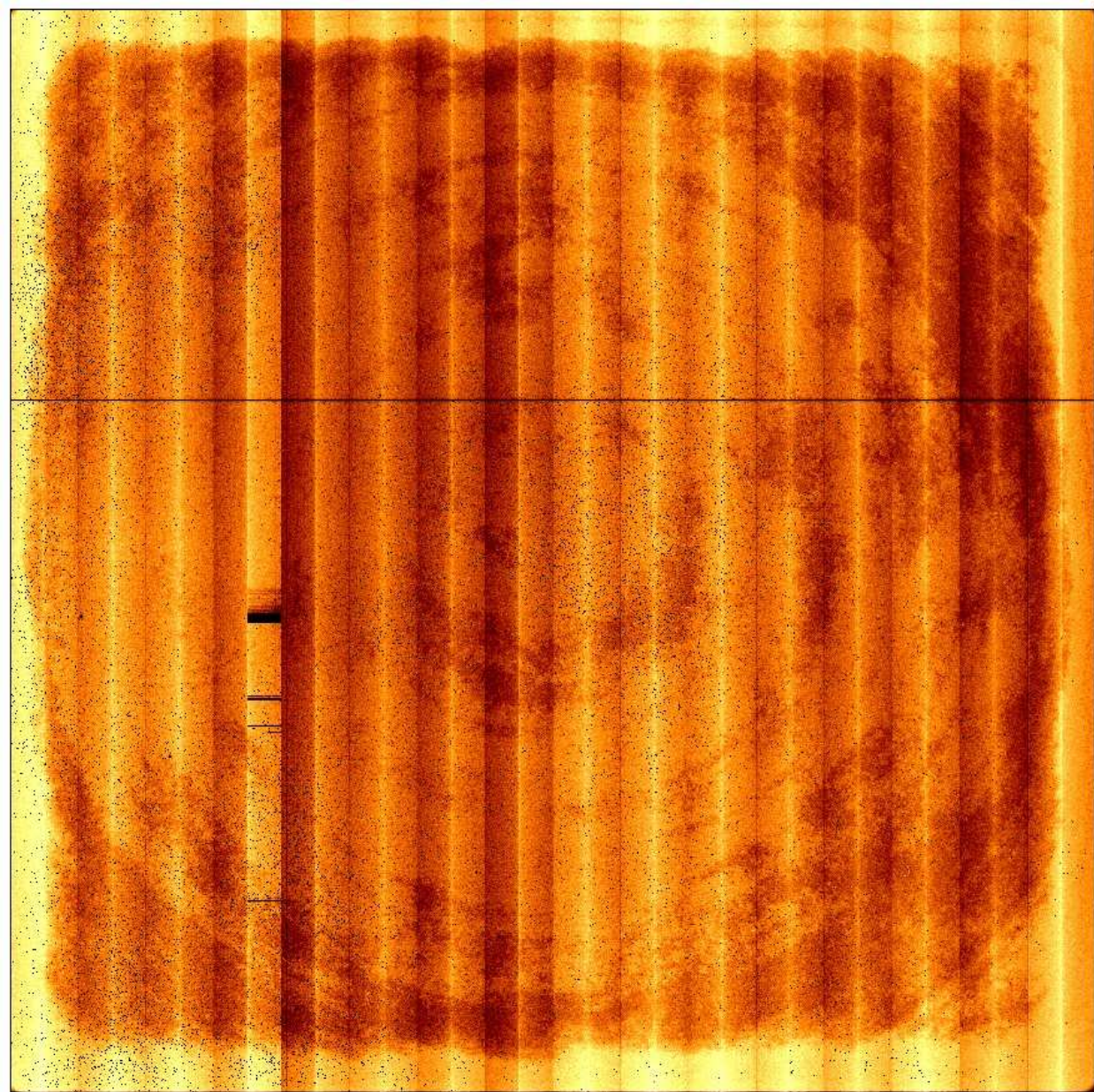
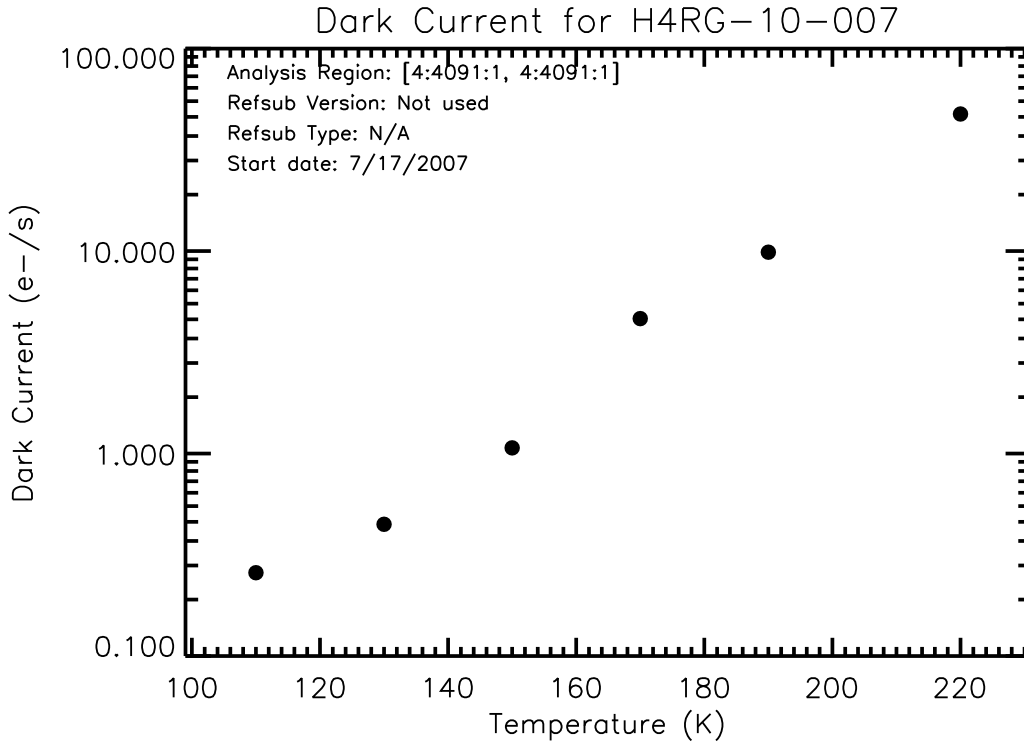


Figure 6. Saturated image. The numbers on the color scale are in ADU and can be multiplied by 2.5 to convert to electrons. The dark pixels correspond to the open pixels and have low quantum efficiency. The electronics for output column 8 (from the left) had intermittent connection that produces artifacts not related to the detector.

2.6 Dark Current

We measure dark current as a function of temperature for each pixel by fitting a linear slope to the increasing signal values in a sequence of non-destructive reads "up-the-ramp." Figure 7 shows the median dark current versus temperature for the H4RG-10-007 device. Figure 8 shows a similar plot for the devices we have measured, where the dark current has been converted into a density to account for the 10 micron pixel size of the H4RG-10-007 device and the 18 micron pixel size of the other devices. Note that the dark current density for the H4RG-10-007 device is relatively high and its dependence on temperature is relatively weak.



E:\H4RG-10-007\cold2\ASIC\darkcurrent_test.17Jul07\gain=1\noref\SlopePlots\darkjumbo_versustemp_H4RG-10-007_electron

Figure 7. Dark current versus temperature for H4RG-10-007.

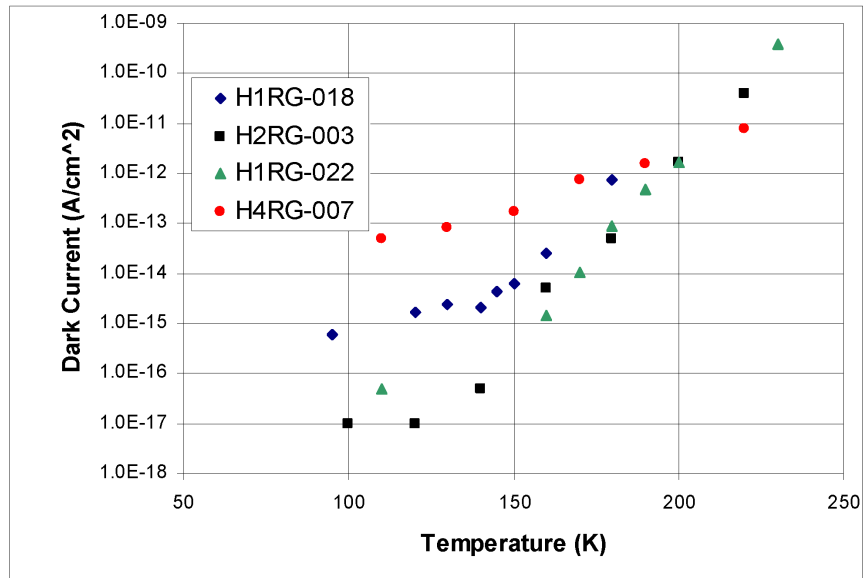


Figure 8. Dark current versus temperature for H4RG-10-007 along with several other HxRG detectors.

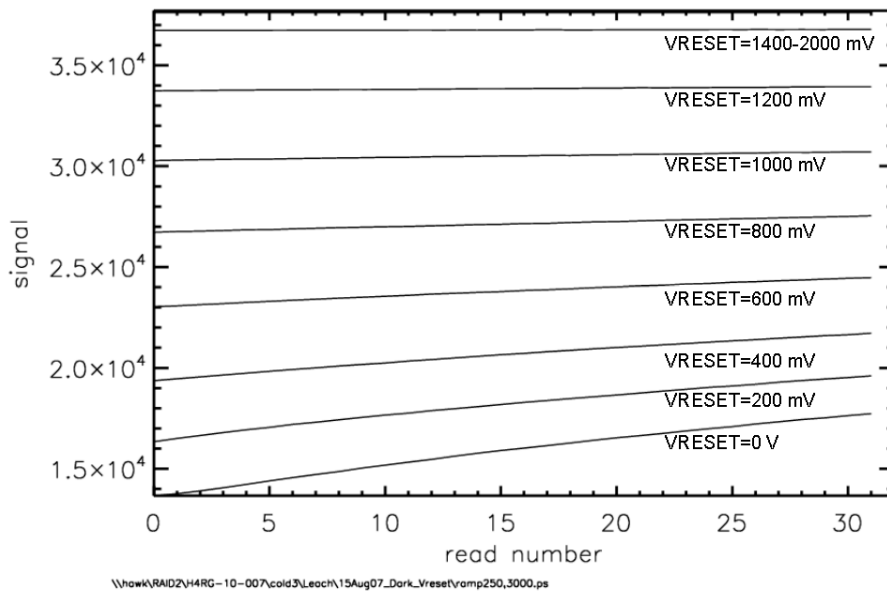


Figure 9. Curves of raw signal versus read number for a single pixel with increasing VRESET toward the top. The top few curves are overlapping. The apparent dark current is going down with increasing VRESET, to the point where it is non-existent for the highest VRESETs.

2.7 Read Noise

We measure the read noise as the standard deviation of signal values for a population of pixels distributed over a spatially contiguous region in the absence of illumination and dark signal. The measurement requires that the detector temperature be low enough and exposure time be short enough to prevent significant dark current from accumulating and contributing shot noise to the standard deviation. In addition, the off-chip electronics must have low enough noise such that it also does not contribute to the standard deviation.

The dark current ramps contain the data that we use for measuring read noise. We process the data by averaging groups of adjacent reads to form "Fowler pairs".⁶ In general, the standard deviation appears to decrease as $1/\sqrt{N}$, where N is the number of Fowler pairs. Deviations from this behavior suggest $1/f$ noise, or contamination by shot noise from dark current.

We find CDS read noise of about $15 e^-$. Once the system read noise is subtracted in quadrature, we find a device read noise of about $13 e^-$.

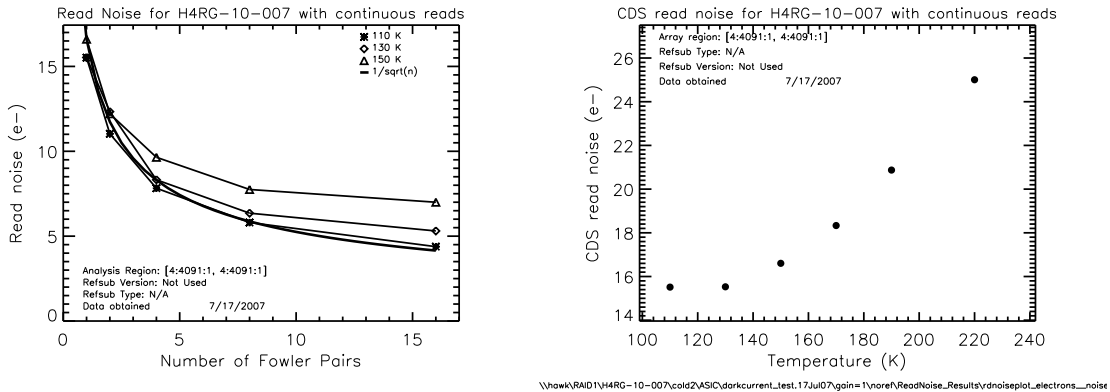


Figure 10. H4RG read noise versus Fowler pair (left), and total noise versus temperature (right). Note that shot noise from dark current begins to make significant contributions to the total noise for temperatures greater than approximately 160 K.

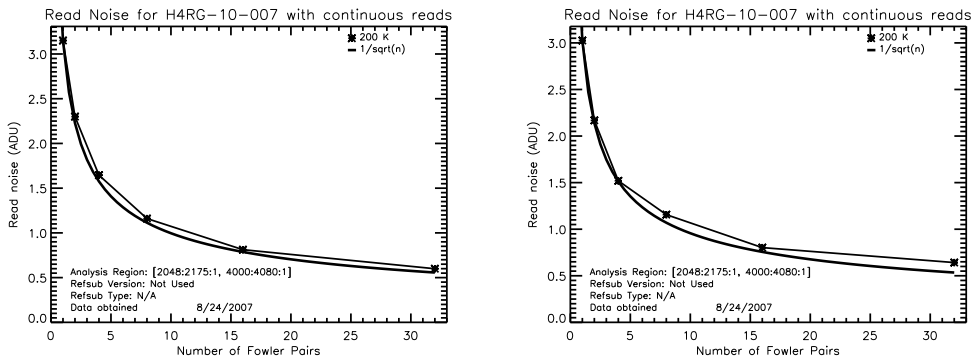


Figure 11. System noise in ADU. (left) Shorted-input noise measured with the ARC electronics with gain of 1.8 ($2.3 e^-/\text{ADU}$). (right) The plot was generated by taking data with the ARC electronics connected to the detector and with the detector reset switch closed during reading. Therefore, it includes all sources of noise except the indium bump and the light sensitive layer of the detector. Note that both plots are about the same, suggesting that the ROIC does not contribute much noise to the measurement.

2.8 Detective Quantum Efficiency (DQE)

DQE is the realized S/N compared to that of an ideal detector. It is often measured in the background-limited case so that it is most closely related to the photon capture process in the bulk material of the detector, as opposed to being related to read noise effects in the post-capture electronics. DQE can vary with wavelength, temperature, and individual pixel properties, to name a few examples. In the RIDL experiment, we illuminate the detector with a monochromatic flat field produced by an integrating sphere and monochromator. The light is monitored by a calibrated silicon photodiode located at a port on the integrating sphere. In future testing, a similar calibrated diode will be placed at the location of the detector in order to transfer the flux measured at the integrating sphere to the focal plane. Once this wavelength-dependent calibration is made, the detector will then be placed at the focal plane and the experiment repeated.

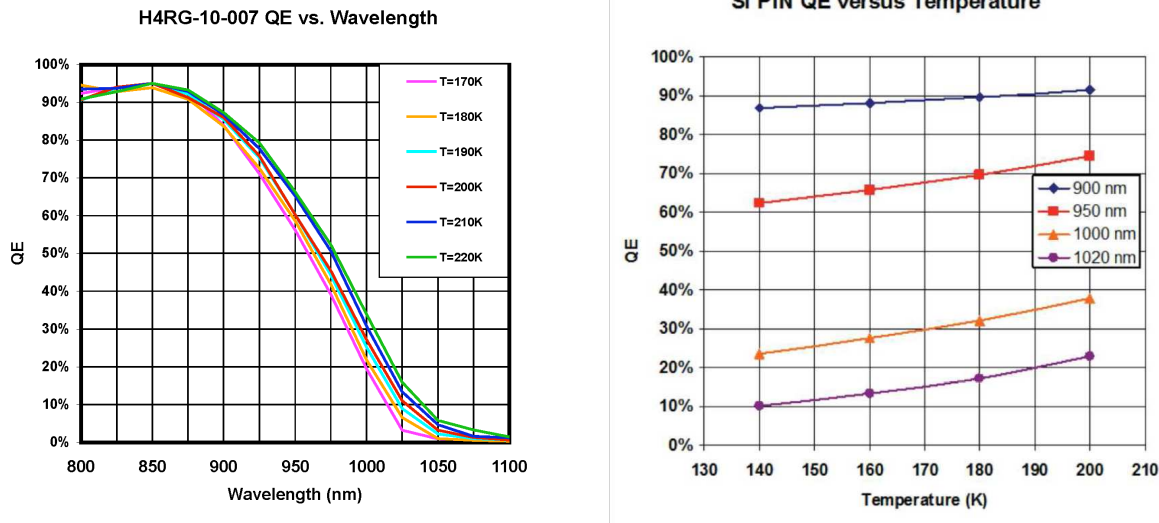


Figure 12. H4RG-10-007 relative QE versus wavelength (left) and H2RG-003 relative QE versus temperature (right) near the long wavelength cutoff. The results show that QE increases with temperature and are consistent with a silicon detector having 100 μm thickness.

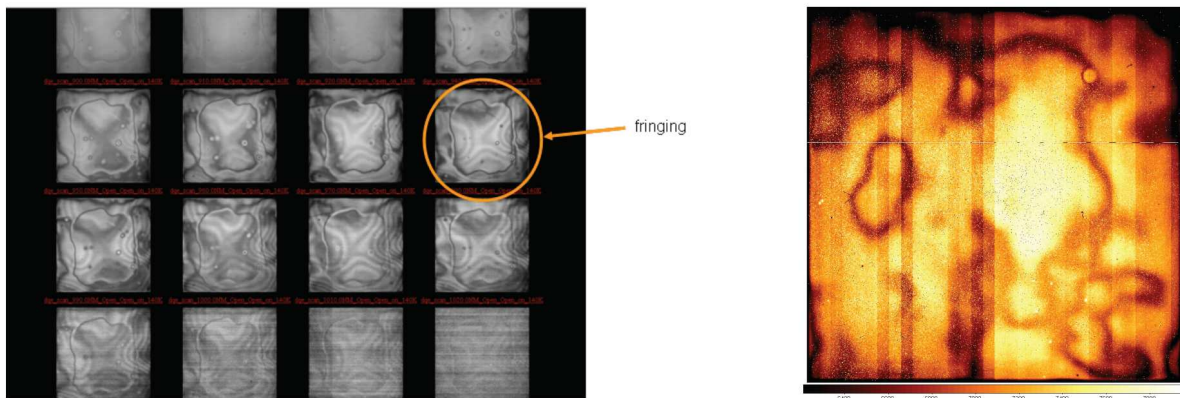


Figure 13. Fringing seen in monochromatic flat field images near 1 μm obtained with the H2RG-003 device (left). The fringing indicates thickness variation of a few microns. Fringing for the H4RG-10-007 device (right). The columnar striping is an artifact of electronic readout offsets and is not a QE variation of the detector.

2.9 Pixel Behavior Vs. VSUB

VSUB sets the backside contact voltage and, along with DSUB, defines the electric field strength in the bulk. Figure 15 shows the behavior of the median dark current across the array for three values of VSUB: 0 Volts, 5 Volts, and 30 Volts. In the first case, photogenerated charge in the bulk is under no force to migrate toward the charge collection node. Because of this, little charge is integrated. Note, though, that there are still many hot pixels, suggesting that charge generation in hot pixels is localized near the charge collection node. At VSUB=5 Volts, charge integrates on the collecting node, but there is significant lateral diffusion. This is to be expected, as the electric field is not strong enough to provide full depletion. At VSUB=30 Volts, the effective point spread function is much tighter.

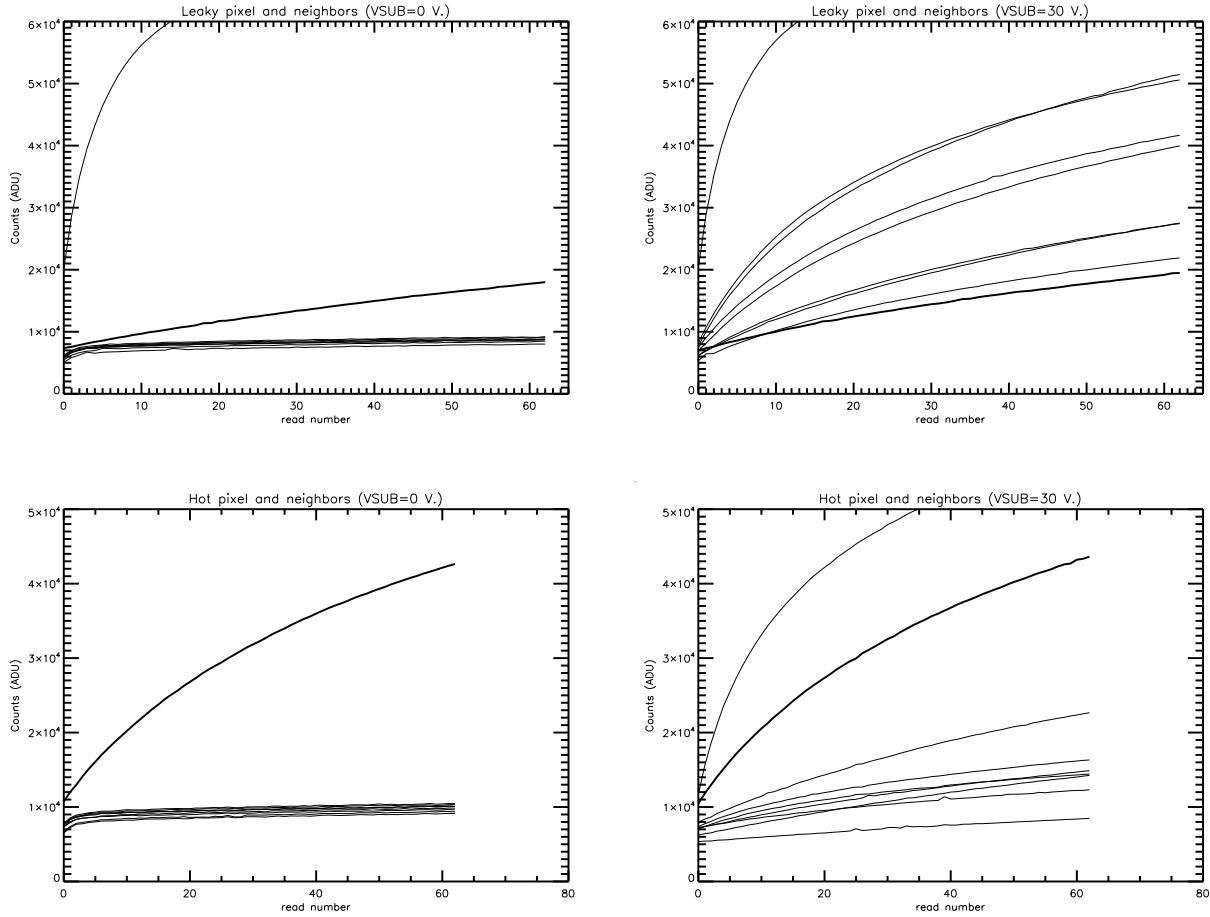


Figure 14. Signal versus read number for open (upper) and hot pixels (lower) under no voltage (left) and 30 Volt (right) levels for VSUB. The bold lines refer to a central pixel, and the remaining eight lines are for the nearest neighbors. Both open and hot pixels have constant behavior versus VSUB. At high VSUB, charge generated in the open pixel migrates to neighbors. Note that one of the open pixel neighbors is hot, and one of the hot pixel neighbors only becomes hot as voltage is applied to VSUB.

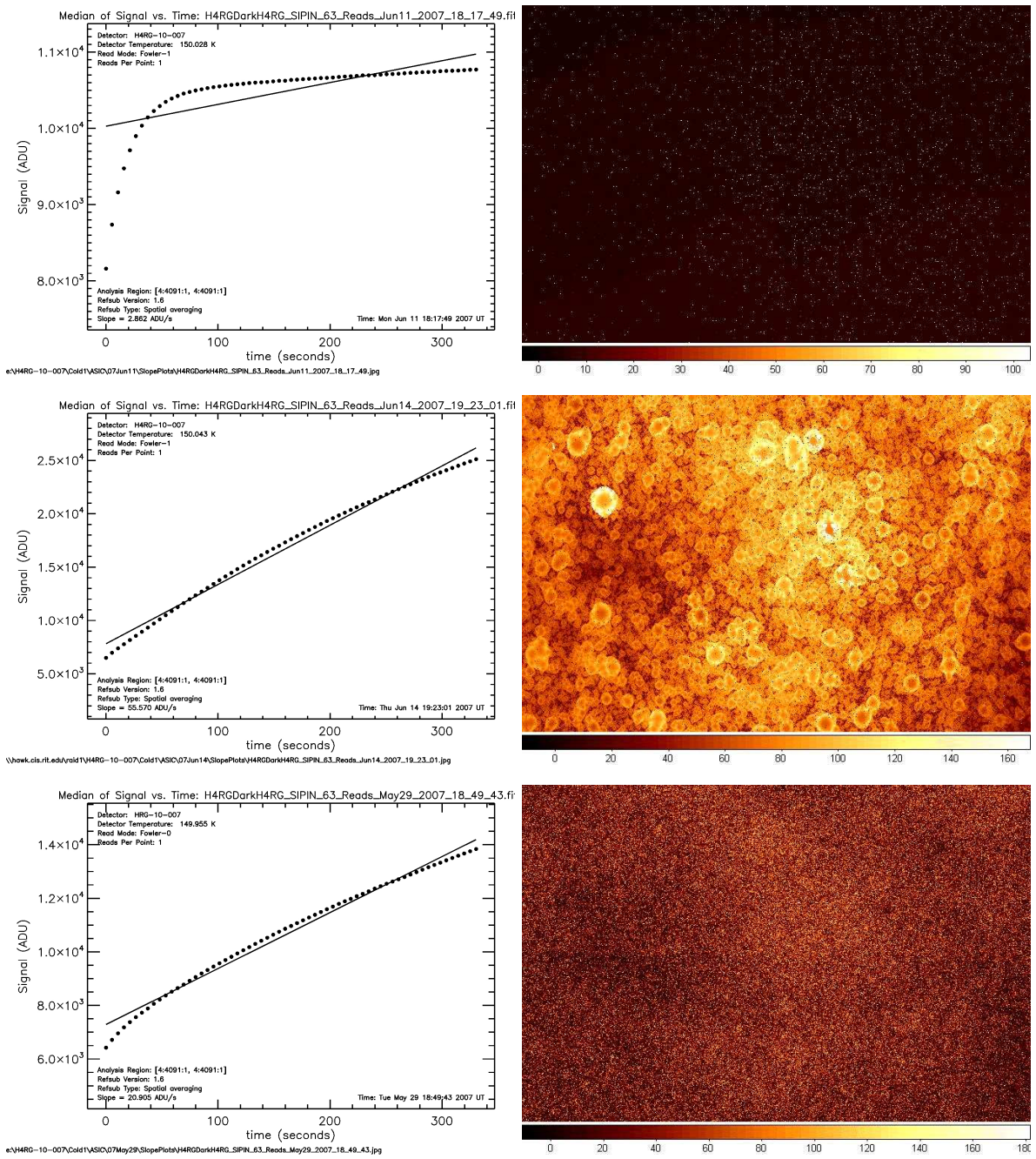


Figure 15. Median dark current and images versus VSUB (0 Volts, top, 5 Volts, middle, 30 Volts, bottom). Hot pixels appear extended at VSUB=5 Volts because the bulk is not fully depleted.

2.10 Window Mode

We exercised *window mode* using multiple sized windows. Figure 16 shows signal versus time extracted from a window of a dark image. The estimated CDS noise is 15 electrons, and the power is white. The noise can be averaged down as $1/\text{root}(n)$, where n is the number of reads.

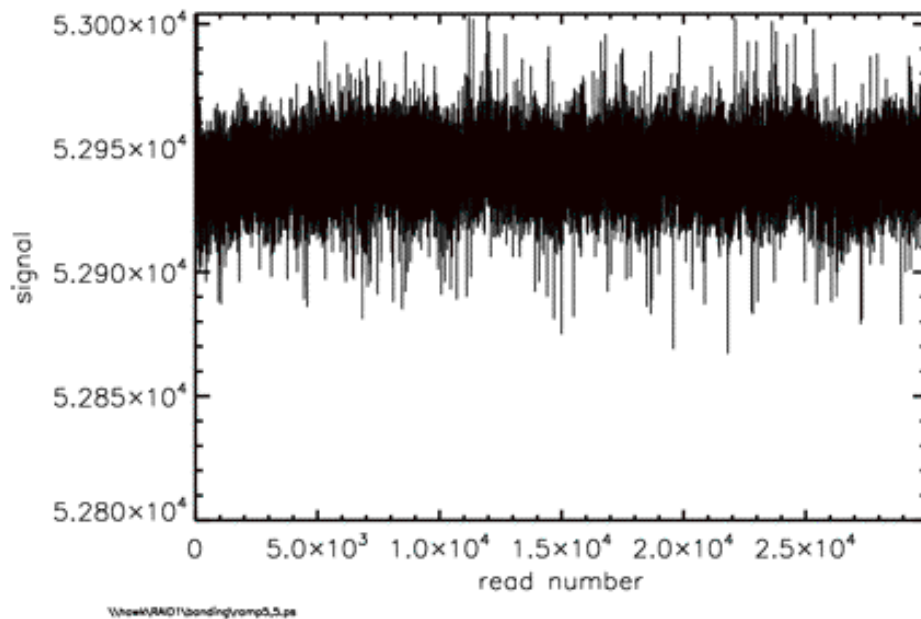


Figure 16. Signal (ADU) versus read number for a pixel in a 10x10 window centered on pixel 505,505 of the H4RG-10-007. The gain is 1 electron per ADU, and the CDS read noise is 15 electrons. The noise is white, although the signal appears to increase slightly just after reset, akin to the reset anomaly typically seen in hybrid devices.

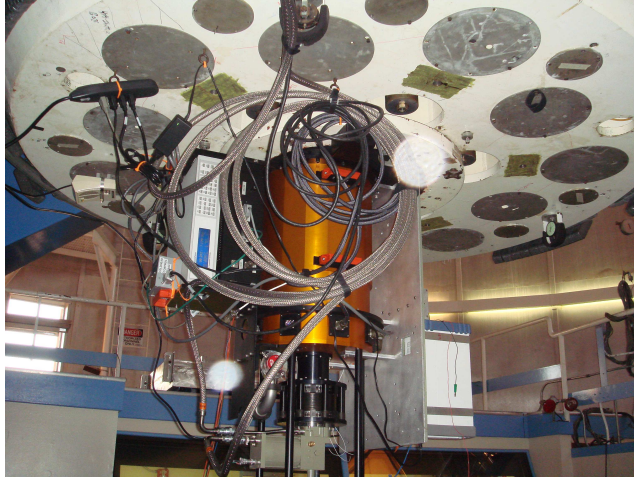


Figure 17. A photograph of the RIDL dewar mounted to the Kitt Peak 2.1m telescope.

3. OBSERVATIONS

We observed on the 2.1m telescope at the KPNO observatory in Tucson, Arizona ($110^{\circ} 58' 0''$ W, $32^{\circ} 13' 0''$ N) during the nights of 4/25/2007-5/1/2007. A picture of the RIDL dewar and electronics mounted to the telescope is shown in Figure 17. With an f7.6 beam and 10 micron pixels spanning a 40.96×40.96 mm array, the plate scale was approximately $0.126''$ per pixel and the field of view was $8' \times 8'$. The H4RG detector was housed inside the RIDL dewar and positioned behind a filter wheel with six positions controlled by Phytron motors. Two of the positions were left open, one was a blank that prevented light from reaching the detector, and the other three were occupied by g , i , and y filters, described in Table 3. To accommodate the RIDL dewar, the telescope guider camera was removed from the telescope. The telescope was set to track at the sidereal rate and a rotator was used to correct for rotations of the field of view.

During our observations at the telescope, a stray signal was present somewhere in the electronics and this gave rise to "pseudo-random" noise that appeared in our images. The source of the signal was traced to a USB to optical fiber converter device, but attempts to remove it proved futile. We refer to it as "pseudo-random" because the oscillations in the electrical signal were not in sync with the reading of the electronics and so it appeared different in each image, but the temporal power spectrum was very repeatable throughout our observations. A typical power spectrum and signals from each of the nights are shown in figure 18 below. There is very little power at frequencies above 40 Hz.

Since one of the 32 inputs on the SIDECAR ASIC was not sensitive to the analog signal coming from the 0th output of the H4RG, we chose to use this entire channel in addition to the reference columns on the left and right side of the detector to attempt removal of the common mode noise. This task has proven difficult, however, since the scale of the fluctuations seems to vary over the detector. Unfortunately, the signature is still apparent in our science images.

Table 3. Filter Characteristics

Filter Name	Peak (nm)	Cuton (nm)	Cutoff (nm)	Transmission (%)
g	476	401.22	557.87	96.39
i	742	667.61	815.77	96.14
y	1003	970.54	1036.01	86.28

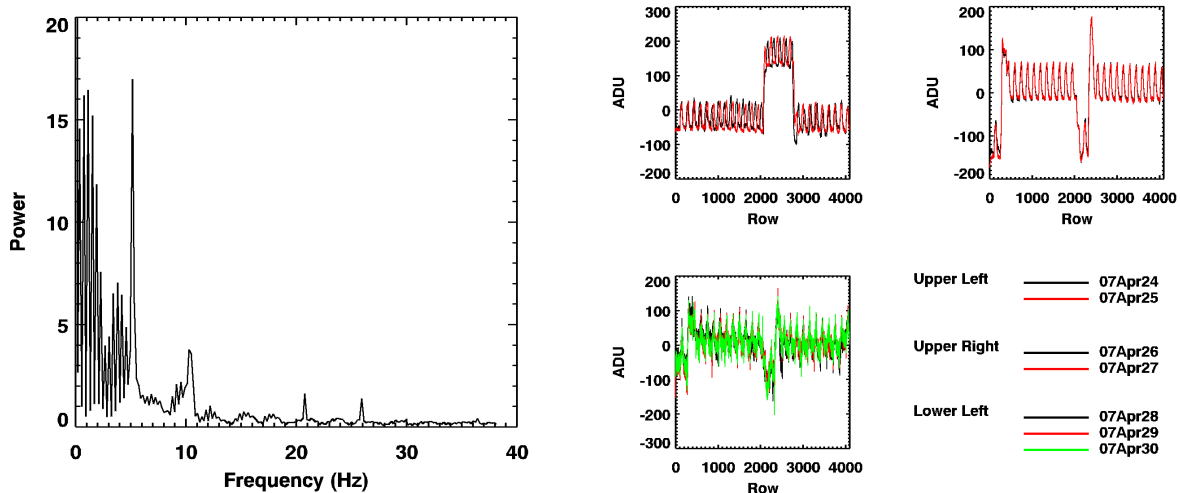


Figure 18. (Left) Average power spectrum of all 128 channels corresponding to output 0 of the H4RG detector. (Right) Deviation of the median of each row in Channel 0 from the mean of Channel 0.

Our observations consisted of *full frame* exposures – ones in which we clocked through every pixel in the detector one or more times – and *window mode* exposures – ones in which we clocked through only the pixels in a sub-region of the detector one or more times. The full-frame mode is well suited for long exposures of faint objects and the *window mode* is more appropriate for high speed photometric measurements or telescope guiding. Each will be discussed in turn.

3.1 Full Frame Mode

A diagram that illustrates a *full frame* ramp sequence is shown in figure 19.

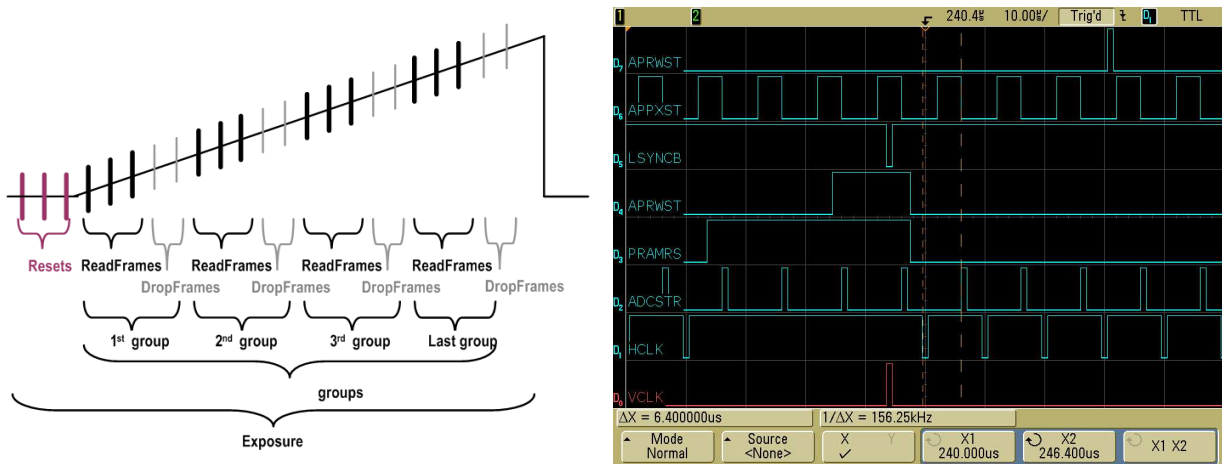


Figure 19. (Left) An illustration of the ramp sequence, courtesy of Markus Loose. The number of resets, drops, groups, and reads are programmable in software, allowing control over the exposure time. (Right) An oscilloscope trace of several clock lines on the SIDECAR ASIC. The delay time t_{rs} is visible.

The ramp consists of a series of N frames, the basic unit in which the entire array of pixels is clocked through. The clocking scheme is similar to the one employed in CCDs, with a fast direction along the rows controlled by a horizontal clock (HCLK) and a slow direction along the columns controlled by a vertical clock

(VCLK). The duration t_f of the *frame* is determined by the pixel time t_p , which corresponds to the time between edges of the HCLK signal configurable on the ASIC, and the number of outputs N_o used on the H4RG, each of which is paired with an input on the SIDECAR ASIC. It is roughly $t_f = t_p * 4096 * 4096 / N_o + 4096 * t_{rs}$, where t_{rs} is a time associated with moving to the next row of $4096 / N_o$ pixels in the array. t_f is also the time between reading a pixel in one *frame* and reading that same pixel again in the following *frame*. The SIDECAR ASIC we used had a maximum of 36 inputs, so we chose $N_o = 32$, and we used a $10 \mu s$ pixel time, giving $t_f = 5.24288s + 4096 * t_{rs}$. Eventually, we implemented a counter on the SIDECAR that allowed us to precisely measure a *time* of $t_f = 5.453s$ and $t_{rs} = 52\mu s$. This was also verified on an oscilloscope, the trace of which is shown in Figure 19.

The illustration shows three different types of *frames*: *reset frames*, *drop frames* and *read frames*. During the *reset frames*, the array is clocked so that the gate of the reset FET in the ROIC pixel is enabled and the pixel is held at the voltage VRESET supplied by the SIDECAR ASIC. This allows the charge on the capacitive node in the silicon to dissipate so that it is ready for a subsequent integration. In the *read frames*, the column select and row enable signals for all of the pixels are enabled in turn, bringing the voltage at a pixel to its corresponding output FET. This voltage is converted to a digital number and sent out to the Data Acquisition System (DAQ) for recording. The unique feature of the *drop frames* is that no data is output from the SIDECAR to the computer. This allows the user to take a very long exposure without dealing with overwhelming amounts of data. It should be mentioned that data from the *reset frames* can be output to the external DAQ and the pixels can be clocked during the *drop frames* by writing to registers on the SIDECAR ASIC.

In a fashion similar to the scheme used in the NICMOS and JWST specifications,⁷ we refer to a ramp having a cadence of N_{rs} *reset frames*, N_d *drop frames*, N_g *group frames*, and N_{rd} *read frames*, as a $N_{rs}-N_{rd}-N_d-N_g$ ramp. Such a ramp has a total of $N_g \times N_{rd}$ data frames. With these definitions, the exposure time of a ramp in *full frame* is given by

$$t_e = N_g * (N_d + N_{rd}) * t_f, \quad (4)$$

with t_f being the frame time given above. To avoid confusion in the following sections, we will use this syntax and reserve the terms *ramp* or *exposure* for such a sequence. We will use the terms *read* or *frame* to describe a *read frame* in these ramps. And the term *image* will be used to refer to the data produced after reduction of these *ramps*, which is described in the next section.

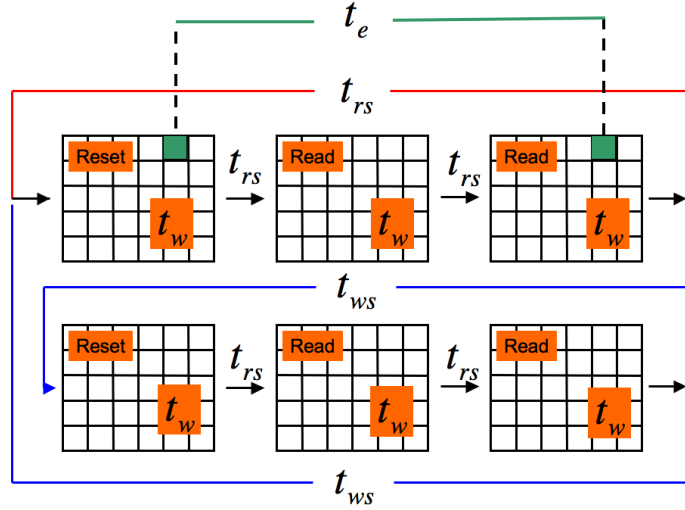


Figure 20. An illustration showing the sequencing and times (described in text) involved with *window mode*. The line labeled t_{rs} at top shows the path taken in *single window mode* and the line labeled t_{ws} line shows that taken in *multiple window mode* when $N = 2$ windows are used.

3.2 Window Mode

The H4RG contains a serial register that can be configured to allow random access to a contiguous $X \times Y$ subset of pixels, or window, through one output of the detector. X and Y , the number of columns and rows in the window, respectively, must be greater than 1 pixel and less than 1024 pixels. Programming the addresses of the window limits, X_{start} , X_{stop} , Y_{start} , and Y_{stop} , can be done on the fly. This allows multiple windowed regions of the detector to be read out in a ping-pong like fashion and also the possibility of feedback control loops in which the window coordinates are continually adjusted to track an object. We used the window mode functionality for three purposes: (1) to focus the telescope in real time, (2) to observe objects that were suspected to vary on short timescales ($< 1s$), and (3) to collect data on absolute and differential image centroid motion across our $8' \times 8'$ field of view.

Our basic unit in a *window mode* observing sequence is a correlated double sample in which we clocked through all $X * Y$ pixels in a window 3 times, resetting each pixel once and then reading the pixel voltages twice. The clocking is similar to full frame mode, with the fast clocking along the rows and the slow clock along the columns. With a pixel time of t_p , one row takes $X * t_p$ seconds with an additional t_{rs} seconds of overhead in shifting to the next row. To complete all rows thus requires $t_w = Y * (X * t_p + t_{rs})$ seconds and this is the total time for a reset or a read in the window sequence. An effective exposure time for a CDS in *window mode* is given by

$$t_e = 2t_w + 2t_{rs}, \quad (5)$$

the time between the reset of a pixel and sampling it in the second read. For our observations, we used a pixel time of $t_p = 10\mu s$ and minimized the overhead to attain $t_{rs} = 18\mu s$. t_p can be decreased in order to decrease the time to complete one CDS sequence and up the sampling rate with a penalty in noise.

After a CDS sequence, either another CDS is repeated on the same window or the serial register is programmed with a new set of window coordinates. We refer to the former as *single window mode* and the latter as *multiple window mode*. With the microcode used on the SIDECAR ASIC, the operation of writing new window coordinates for X_{start} , X_{stop} , Y_{start} , and Y_{stop} takes $t_{ws} = 150\mu s$; adjusting only two of these four would take $\sim 75\mu s$. A diagram showing the times associated with window mode is shown in Figure 20. It should be apparent from the diagram that if N windows are used in *multiple window mode*, the time it takes to complete a full cycle

and return to the first window is given by:

$$t_c^{mw} = 3Nt_w + 2Nt_{rs} + Nt_{ws} \quad (6)$$

And if *single window* mode is used this time becomes:

$$t_c^{sw} = 3(t_w + t_{rs}) \quad (7)$$

It is also important to know the time between exposures in different windows for the purposes of measuring temporal correlations. In *multiple window* mode, the time it takes between a CDS in window n and a CDS in window m is given by

$$t_{nw} = 3(m - n)t_w + 2(m - n)t_{rs} + (m - n)t_{ws} \quad (8)$$

The full cycle is repeated M times in one full observing sequence, giving a total time of $M * t_c^{mw}$ in *multiple window* mode and $M * t_c^{sw}$ in *single window* mode.

While taking window data in both single and multiple modes at the telescope, the bias subtracted images were displayed on screen via a graphical user interface, and the contrast of signal to background was quite encouraging. However, due to a software error, the first read in our *multiple window* exposures were not saved; only the zeroth read was. This makes the contrast in the saved data of much poorer quality. We will present results from the *single window* mode data as an indication of the signal to noise ratio that should be achievable for both modes. And despite the noisy nature of the *multiple window* mode data, we will use it to highlight the potential of the H4RG to track centroid motion across a large field of view by considering only very bright objects for which the zeroth read still provides an ample signal to noise ratio.

4. DATA REDUCTION

4.1 Full Frame Mode

Each night before we observed we took a set of 1-0-2-1 flat-field ramps through each filter and each morning a set of dark ramps that matched the cadence of the ramps that we had used in our exposures during that night. For each of these ramps, the first read (bias) was subtracted to eliminate kTC noise and a median filter was applied to each set to reject cosmic rays and outliers. This operation yielded one median flat-field ramp with pixel values $I_{flat}^l(x, y, r)$, for each filter l and one median dark ramp with pixel values $I_{dark}(x, y, r)$ for each cadence.

4.1.1 Dark Subtraction

From each exposure of the sky through a given filter we subtracted a median dark ramp of the same cadence for each pixel, i.e $I_{obj}(x, y, r) = I_{lum}(x, y, r) - I_{dark}(x, y, r)$, where I_{lum} is the pixel value from the illuminated image. The resulting frames in this ramp should, in theory, have pixel values I_{obj} that correspond to luminance from the source being observed.

4.1.2 Slope Fitting

Although the dark current signal I_{dark} and illuminated signal I_{lum} on H4RG-10-007 appear to be nonlinear with respect to time, the difference $I_{lum} - I_{dark}$ shows good linearity over a large fraction of the full well. Figure 21, generated from the median of a set of 30 1-0-30-1 y band ramps in which the detector was uniformly illuminated, is indicative of this. It shows a plot of the average of the normalized slopes $m_n = (I_{obj}(x, y, r) - I_{obj}(x, y, 0))/t(r)$ at a given ADU value, $I_{lum}(x, y, r)$, vs. ADU value, with $t(r)$ being the time at read r . The normalization is made on a per pixel basis by finding the slope, $m_o = (I_{obj}(x, y, r_{max}) - I_{obj}(x, y, r_{min})) / (t(r_{max}) - t(r_{min}))$, that minimizes the quantity $Err = \sum_1^N abs[I_{obj}(r) - (m_o * t(r) - b_0)]$ for all values of t before I_{obj} reaches its maximum value in the ramp. r_{max} and r_{min} are different for different pixels, but average values are $r_{min} = 5$ and $r_{max} = 22$. As indicated in the figure, on average the slope of each ramp deviates by less than 5% from m_o over 85% of the full ADU range. Nonlinear effects appear in the lowest 8.25% ADU values and the uppermost 6.4% ADU values. A more proper treatment would be to obtain lower and upper limits like this for each pixel by collecting data at many different levels of illumination and exposure times. We plan on doing this in a future experiment.

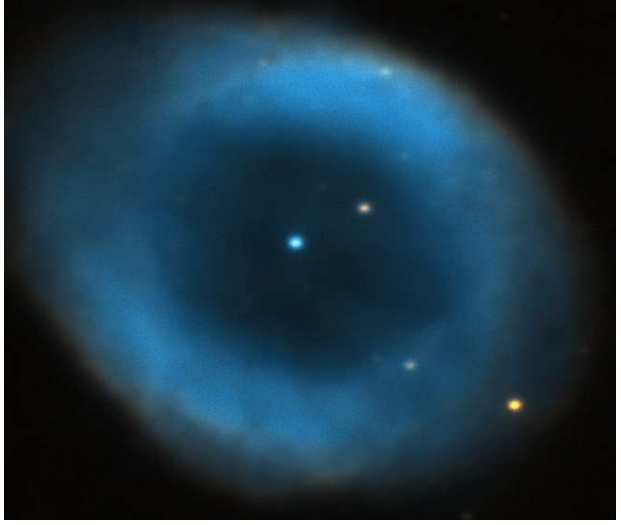
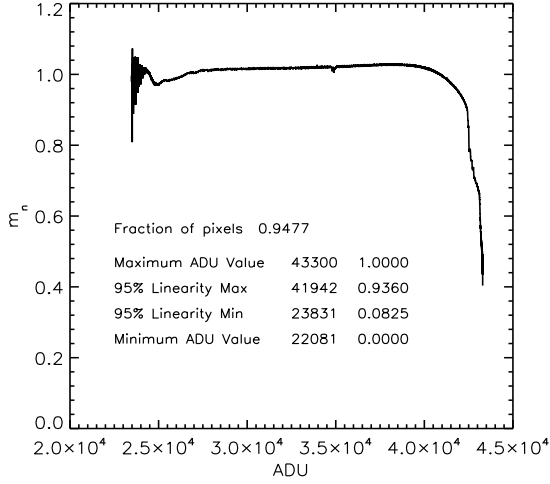


Figure 21. (Left) Linearity of the H4RG on the night of 4/27/07 with a gain of 1. (Right) A 650x550 pixel cut-out from a false-color image of M57 made by combining the reduced images from the g and i filters.

The slope m_o is useful for determining ADU values I_{lum}^{min} and I_{lum}^{max} between which the ramps are most linear. However, m_o does not provide the best estimate of the true slope within these limits for each pixel since it is constrained to contain two points in the ramp. In order to find the slope that minimizes the error for the points in the linear regime, i.e. where I_{lum} lies between I_{lum}^{min} and I_{lum}^{max} , we fit a line to the corresponding values of I_{obj} using the technique described in Numerical Recipes.⁸ Namely, for a pixel that has $N_{rd} = r_{max} - r_{min}$ values of $I_{lum}(r)$ between reads r_{min} and r_{max} , and corresponding dark subtracted values $I(r) = I_{obj}(r)$,

$$b = \frac{\sum_{r_{min}}^{r_{max}} t(r)^2 \sum_{r_{min}}^{r_{max}} I(r) - \sum_{r_{min}}^{r_{max}} t(r) \sum_{r_{min}}^{r_{max}} t(r) I(r)}{N_{rd} \sum_{r_{min}}^{r_{max}} t(r)^2 - \left(\sum_{r_{min}}^{r_{max}} t(r)\right)^2}, \quad m = \frac{N_{rd} \sum_{r_{min}}^{r_{max}} t(r) I(r) - \sum_{r_{min}}^{r_{max}} t(r) \sum_{r_{min}}^{r_{max}} I(r)}{N_{rd} \sum_{r_{min}}^{r_{max}} t(r)^2 - \left(\sum_{r_{min}}^{r_{max}} t(r)\right)^2}. \quad (9)$$

b is an approximation to the bias offset in ADU, and m is the number of ADU/s attributed to the source of illumination. It should be apparent that only the difference in times $t(r)$ and $t(r+1)$ matters, so it suffices to use the average time for the r th read. With a slope obtained and the proper conversion gain in e^-/ADU , m can be converted to units of e_-/s .

Bright objects will induce saturation very quickly, and in some cases there will be too few or no values of $I_{lum}(r)$ in the linear regime. These cases require alternative approaches. If a pixel is saturated in the first read (the bias read is considered the zeroth read) and $I_{lum}(0) < I_{lum}^{max} - 0.5I_{lum}^{FR}$, where $I_{lum}^{FR} = I_{lum}^{max} - I_{lum}^{min}$, the slope is approximated by the CDS value $m = (I(1) - I(0))/(t(1) - t(0))$. And if a pixel is saturated in the first read and $I(0) > I_{lum}^{max} - 0.5I_{lum}^{FR}$, the best one can do is approximate the slope by $m = I(0)/t(0)$.

Once a slope has been fit to the points in the linear regime, cosmic rays are detected as large deviations from the fit using the same method as the one in the NICMOS reduction code.⁹ In this method, the difference between the data points and the fit is first computed as $D(r) = I(r) - (b - mt(r))$. Then the difference between adjacent points in this difference is taken, $DD(r) = D(r) - D(r-1)$ along with its standard deviation, σ_{DD} . Cosmic rays are flagged as points where $DD(r) > T_r \sigma_{DD}$, where T_r is some threshold. For our H4RG data, T_r was typically set around 3. The idea behind this scheme is that the cosmic rays particles will release significantly more charge in the pixel over some small time interval than the integrating photocurrent and show up as a large negative to positive spike in D_i . Using a separate σ_{DD} for each individual pixel seems to be quite effective and well suited for treating the variation in pixel sensitivity across the array. If a cosmic ray is detected in a read $r = r_{cr}$ late in the ramp, $r_{cr} > r_{min} + N_{rd}/2$, then the slope is refit using points from $r = r_{min}$ to $r = r_{cr}$. If it is detected early in the ramp, $r_{cr} < r_{min} + N_{rd}/2$, the slope is refit using points $r = r_{cr}$ to $r = N_{rd}$. If enough points are

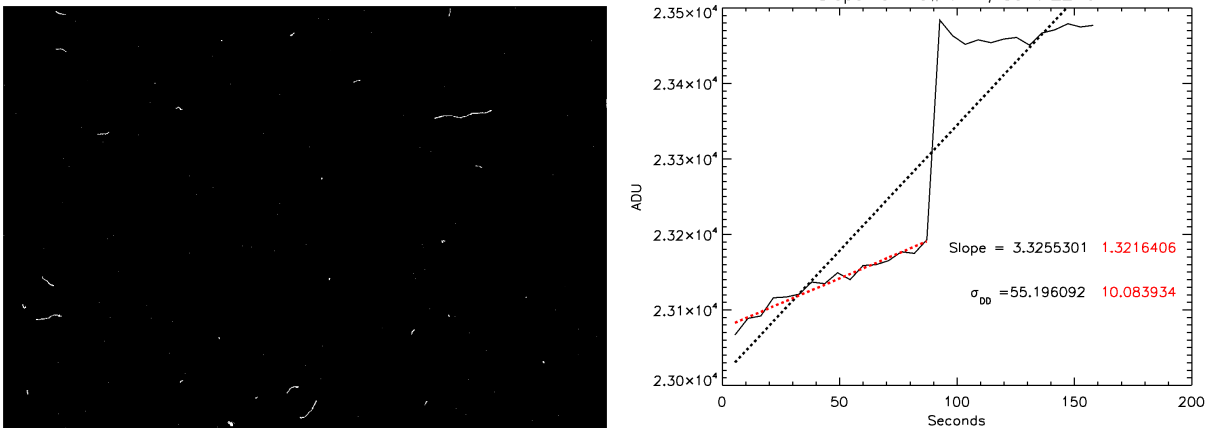


Figure 22. (Left) A section of the cosmic ray image from a 15 read ramp. (Right) Signal vs. time for a pixel that has been hit with a cosmic ray. The black dashed line is the high slope originally fit to the line and the red dashed line is the lower slope after the cosmic ray has been detected in the slope fitting algorithm.

left, another iteration of the cosmic ray detection sequence is performed. The number of points included in the fit is included as an extension to the image for purposes of error analysis.

An added benefit of the up the ramp sampling is that the energy deposited by a high energy particle can be well approximated by examining the signal $I_{r_{cr}} - I_{r_{cr}-1}$. These values are recorded and stored as a separate image. They are potentially interesting for measuring the angular distributions, frequency, and morphology of such events. An example is shown in Figure 22.

4.1.3 Flat Fielding

After every pixel has had a slope fit to it for the exposure, we are left with a 4096×4096 array of slopes, $m(x, y)$, that we take to be the image. This image is divided by the normalized, bias-subtracted, first read $I_{flat}^1(x, y, 1)$ of the median flat-field through that same filter to correct for variation in pixel sensitivity.

4.1.4 Combining Dithers

For our *full frame* exposures, we used a dithering technique to provide a number of samples of each field. The dither pattern was a 3×3 box where each telescope pointing was offset from the previous one by $20''$, or ~ 160 pixels. A full exposure was taken at each of these pointings, giving us 9 slopefitted images of the field in each filter.

The 9 slope images from each filter are aligned using several bright stars and combined into a mosaic. To combine the data from the 1-9 pixel values at a spatial location (x, y) in mosaic image coordinates, we used both a median filter and the mean of the pixels that were not flagged as bad or rejected as 3σ outliers. Using nine images ensured that we had a minimum of three reasonable pixel values in nearly all cases (near the boundaries was an exception), and it was found that the latter method yielded better results than the median filter as it reduces the noise by a factor of $\sqrt{1} - \sqrt{9}$. These mosaics are the images that we use for analysis in the following sections.

4.2 Window Mode

We did not collect dark current data for our *window mode* exposures. This is problematic because the charge that accumulates in a pixel due to dark current in a *window mode* exposure is different from that in a *full frame* exposure since the time between a reset and read of that pixel differs between the two. However, since the sources we observed in window mode were typically very bright, with a magnitude < 13 , $I_{lum} \gg I_{dark}$, we are still able to estimate the signal due to the intensity of the source. In future observing runs, we plan to collect matched sets of darks for all of our *window mode* exposures.

Because of the lack of dark data, the procedure for reducing the window mode data was to subtract the bias read (when available) and divide by the flat-field with matching filter for each CDS sequence. In *single window* mode, this provides a datacube consisting of $M X \times Y$ images at times $t = i * t_c^{sw}$, where $i = 0, 1, 2, \dots, M$. In *multiple window* mode, it provides a datacube of $M X \times Y$ images for each of N windows, sampled at $t = i * t_c^{mw} + t_{nw}$, where $i = 0, 1, 2, \dots, M$ and t_{nw} is calculated from equation 8 using $n = 0$ and $m = 0, 1, \dots, N$ as the index of the window in the sequence of N windows.

5. PHOTOMETRY

To assess the potential of the H4RG as a photometric instrument, we measured instrumental magnitudes of well isolated standard stars in the Landolt Equatorial Fields PG 1530 and SA 109 as well as stars in the crowded field of the M13 cluster. Photometric measurements of Landolt stars is well suited for testing the ability of the detector to sense brightness differences within a particular wavelength passband as well as determining how well it can be calibrated to obtain absolute magnitudes within that band. Crowded-field photometry of the stars in M13 is good for determining the spectral responsivity of the detector by comparing measurements through separate passbands since the relationship of color index vs. magnitude has been well studied in the cluster.

5.1 Aperture Photometry: Landolt Standards

Landolt Standard stars provide a good set of basis measurements for comparison as they have been repeatedly observed through different filter sets with different calibrated instruments. Unfortunately, these standards have been observed very frequently through UBVRI filters of the Johnson-Kron-Cousins system, but not through g, i , and y filters that are more closely matched to our set. It is possible, however, to make a transformation between pairs of filters in these two systems under the assumption that the variation of the spectral energy distribution $E(\lambda)$ of the stars is sufficiently continuous over the intervals considered to allow a Taylor expansion in λ .

Such a transformation is done, as in,¹⁰ by solving the following equations:

$$m_l^{H4RG} = M_j^{CAL} Z - KX + CT \times (M_k^{CAL} - M_j^{CAL}), \quad (10)$$

where M_j^{CAL} is the reference magnitude in the filters $j = V, I, \text{ and } Y$, m_l^{H4RG} is the instrumental magnitude that we measured through the filters $l = g, i, \text{ and } y$, X is the airmass, K is the atmospheric extinction coefficient, CT is a color coefficient and $M_k^{CAL} - M_j^{CAL}$ is the color defined by filter j and $k = B, R, \text{ and } H$ from the reference measurements. Astronomers frequently use these equations in order to compare measurements made at different telescopes and to calibrate for slight differences between filter sets. They are typically solved using a population of several hundred standard stars. Due to limited time and data, we have only seven.

The transformations require a calculation of an average airmass over the duration of our exposures in each filter band. For this we used the algorithm suggested by Stetson¹¹ : $X_{avg} = (X_{beg} + 4X_{mid} + X_{end})/6$, where X_{beg} is the airmass at the beginning of the first exposure, X_{mid} is the airmass midway through the exposure (for us it was the fifth dither in the sequence) and X_{end} was the airmass at the end of the dither sequence. The average airmasses through which we observed ranged from 1.12 to 1.26, so loss due to atmospheric extinction was not very significant.

Once the equations are solved, they can be used to predict the magnitudes we should expect to observe for g, i , and y filters at zero airmass based upon standard magnitudes in $V, I, \text{ and } Y$ and the corresponding colors. The fitting coefficients and errors are shown in Table 5 and a plot that illustrates the goodness of the fit is shown in Figure 23. The errors in the fit are not unreasonable. They are similar to the ones found in the transformations made in the Sloan Digital Sky Survey.¹² The error in g is substantially higher than it is in i and y . This may be attributed to a number of factors including observing conditions, wavelength dependent lateral diffusion in the detector, and nonlinearity. The exact reason for the large discrepancy is still being investigated. However, the data and the fit indicate that the H4RG is capable of doing absolute photometry. In future observations we plan to obtain a larger sample of measurements on standard stars in order to obtain the relative error in the photometry.

Table 4. Landolt Star Magnitudes. Our measured magnitudes are denoted by lowercase m . M are catalogued magnitudes; + are taken from Landolt (1973)¹³, \diamond are taken from Landolt (1992),¹⁴ and \star from Gullixson (1995).¹⁵ All M_Y are from Persson (2002).¹⁶

Star	M_Y^{CAL}	ΔM_Y^{CAL}	$M_Y^{CAL} Error$	$M_Y^{CAL} - M_H^{CAL}$	m_y^{HARG}	Δm_y^{HARG}	$m_y^{HARG} Error$
109-956	12.516	0.000	0.029	1.038	15.362	0.000	0.001
109-954	10.254	2.262	0.028	1.064	13.079	2.283	0.001
109-949	11.384	1.132	0.029	0.595	14.250	1.112	0.001
	M_V^{CAL}	ΔM_V^{CAL}	$M_V^{CAL} Error$	$M_B^{CAL} - M_V^{CAL}$	m_g^{HARG}	Δm_g^{HARG}	$m_g^{HARG} Error$
109-959 \star	12.790	0.000	0.029	0.780	12.404	0.000	0.003
109-956 \diamond	14.639	-1.849	0.011	1.283	14.407	-2.003	0.009
109-954 \diamond	12.436	0.354	0.009	1.296	12.187	0.217	0.003
109-949 \diamond	12.828	-0.038	0.006	0.806	12.408	-0.004	0.002
1530-057 \diamond	14.21	0.000	0.000	0.151	12.756	0.000	0.003
1530-057A \diamond	13.71	0.500	0.000	0.829	12.514	0.242	0.003
1530-057B \diamond	12.84	1.37	0.000	0.745	11.595	1.161	0.002
	M_I^{CAL}	ΔM_I^{CAL}	$M_I^{CAL} Error$	$M_R^{CAL} - M_I^{CAL}$	m_i^{HARG}	Δm_i^{HARG}	$m_i^{HARG} Error$
109-959 +	11.572	0.000	0.009	0.671	12.197	0.000	0.003
109-956 \diamond	13.114	-1.542	0.016	0.743	13.886	-1.689	0.007
109-954 \diamond	10.940	0.632	0.003	0.731	11.391	0.806	0.002
109-949 \diamond	11.708	-0.136	0.003	0.517	12.422	-0.225	0.003
1530-057 \diamond	14.011	0.000	0.000	0.036	12.967	0.000	0.003
1530-057A \diamond	12.842	1.169	0.000	0.412	11.967	1.000	0.002
1530-057B \diamond	12.041	1.970	0.000	0.376	11.160	1.807	0.003

Table 5. Transformation equations obtained from the data in Table 4. The superscripts make explicit the fact that the m_i are the magnitudes that are calculated using equation 10 has been solved.

Transformation	LSF Error	σ
$m_y^{fit} = M_Y^{CAL} + 2.173 - 0.068(M_Y^{CAL} - M_H^{CAL})$	0.0068	0.0096
$m_i^{fit} = M_I^{CAL} - 17.03 + 14.08X + 0.388(M_R^{CAL} - M_I^{CAL})$	0.0724	0.0591
$m_g^{fit} = M_V^{CAL} - 10.57 + 8.025X + 0.502(M_B^{CAL} - M_V^{CAL})$	0.1261	0.1030

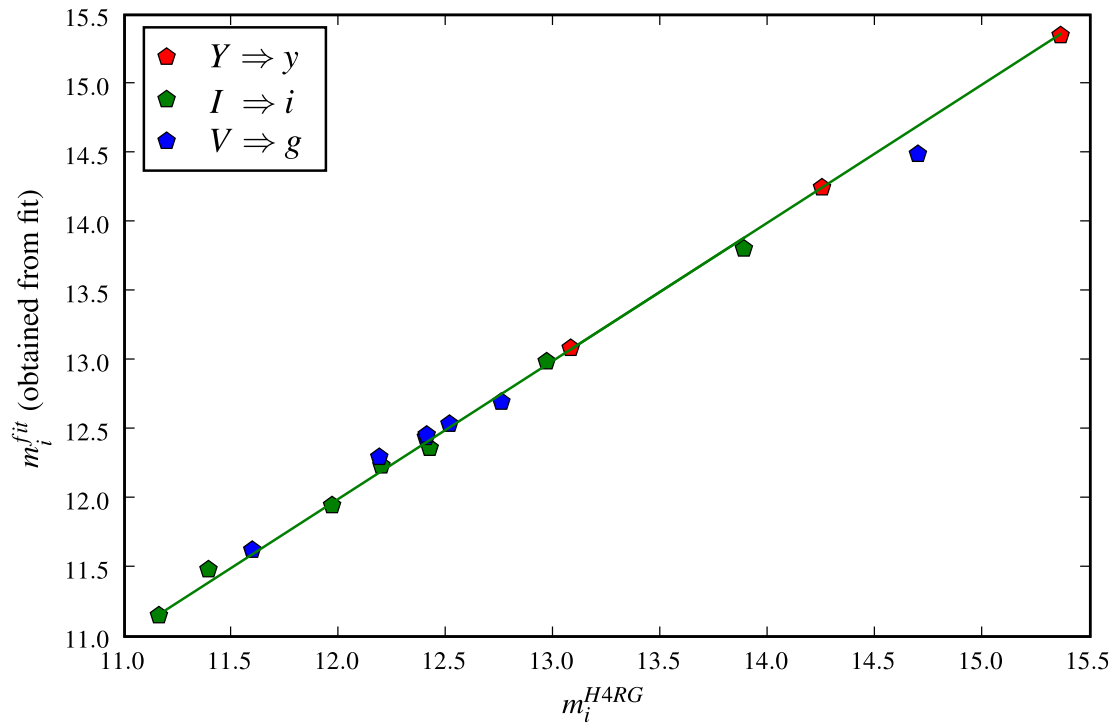


Figure 23. The results from the best-fit solution to the transformation equations. The horizontal axis shows the magnitudes that we measured in our images. The vertical axis shows the magnitudes that are expected from the fits in Table 5 based upon the standard magnitudes. The green line shows where $m_i^{HARG} = m_i^{fit}$.

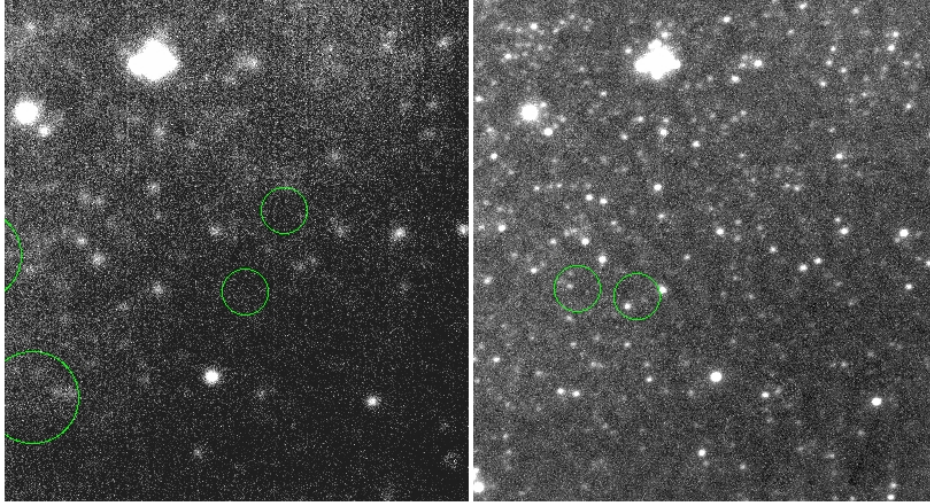


Figure 24. A small section of the slope image mosaics through the I band filter on the outskirts of the cluster. The signal to noise ratio is 5 times higher in the right image from 4/26 than it is in the left image from 4/28.

5.2 Crowded-Field Photometry: M13

We measured instrumental magnitudes of stars in M13 : the Hercules cluster. We observed the cluster in a range of RA from 250.404-250.580 and DEC from 36.368-36.511 on two separate nights : 4/26 and 4/28. As shown in figure 24, the data from 4/26 are of far better quality; the signal to noise ratio of the dim stars is higher by a factor of nearly 5. There are several possible reasons for this. First, observing conditions were better. There was moderately good seeing, no visible clouds, and very little scattered moonlight. On the 28th, there were scattered clouds and the moon was higher in the sky. Second, the ASIC appears to have been better configured. The pre-amps were operating with a gain of 0dB on 4/26 as opposed to 12dB on 4/28. The reduced data with the higher gain appears noisier, suggesting amplification of pre-gain noise in the detector or on the bias voltages supplied by the ASIC to the detector. The trend is similar for the other data as well, making the difference in gain the most likely culprit. Since the data are less noisy and for the sake of brevity, in the following section shows the results from the data taken on 4/26.

The raw data for M13 on 4/26 consists of 9 dithered up-the-ramp exposures for each of the g , i , and y filters and is described in Table 6. Photometric analysis was performed on the slopefitted mosaics of M13 using the DAOPHOT algorithms DAOPHOT, GETPSF, SUBSTAR, NSTAR, and ALLSTAR in IRAF through the PyRAF interface. For details on parameters, refer to appendix B and for a description of DAOPHOT, refer to.¹⁷ The basic purpose of DAOPHOT is to identify point sources and measure the brightness of those sources alone. It does this by allowing the user to create a semi-analytic model that represents the point-spread function (PSF) of a star in the image and goes on to fit each star with that model. This technique is necessary for the case in which the field is "crowded", i.e. the images of the stars are so close that they overlap and a pixel receives light from more than one source. The result of the DAOPHOT algorithms is an instrumental magnitude for each star.

In order to determine the zeropoints of the instrumental magnitudes obtained with the DAOPHOT package, we obtained g and i magnitudes for the stars SDSS J16420106+362401.0 and SDSS J1646154.09+362348.8 from the Sloan Digital Sky Survey and compared them with ours. We find, roughly, that $M_g^{CAL} = m_g^{HARG} - 0.25$ and $M_i^{CAL} = m_i^{HARG} - 0.62$. For y , we use the first equation in Table 5 and set the color term to zero since no stars could be found with y band magnitudes for reference in the field.

With the magnitudes adjusted for the zero point offset, color magnitude diagrams were created for the $g - i$ filter pair and the $g - y$ filter pair. These diagrams are qualitatively similar to those obtained from previous photometric studies for B and V filters. They show well the features of the red giant and blue straggler populations in the cluster. This is a good indication that the H4RG is capable of doing relative photometry between these bandpasses and verifies that the spectral responsivity is good out to the $1\mu m$ region.

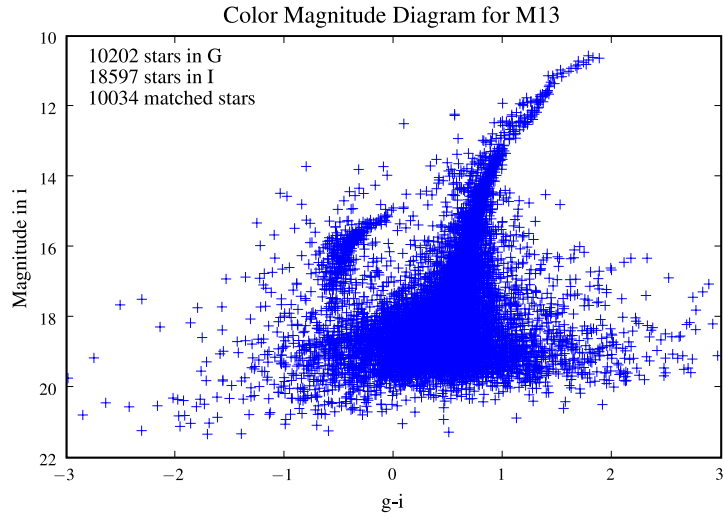


Figure 25. A Color Magnitude diagram for the M13 cluster in g and i bands.

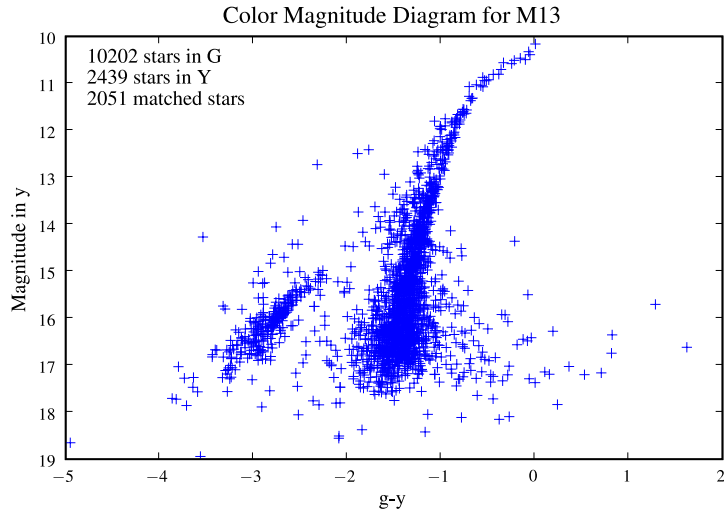


Figure 26. A Color Magnitude diagram for the M13 cluster in g and y bands.

Table 6. Parameters from M13 exposures.

Filter	Airmass	Exp. Time	Cadence (s)	FWHM (")	Avg. Background (counts/sec)	σ Background (counts/sec)	Stars Found
g	1.003909	163.59	1-0-30-1	1.64	2.01	0.38	9104
i	1.011084	81.79	1-0-15-1	1.14	3.05	0.34	15,812
y	1.015034	163.59	1-0-30-1	1.32	1.80	0.28	2439

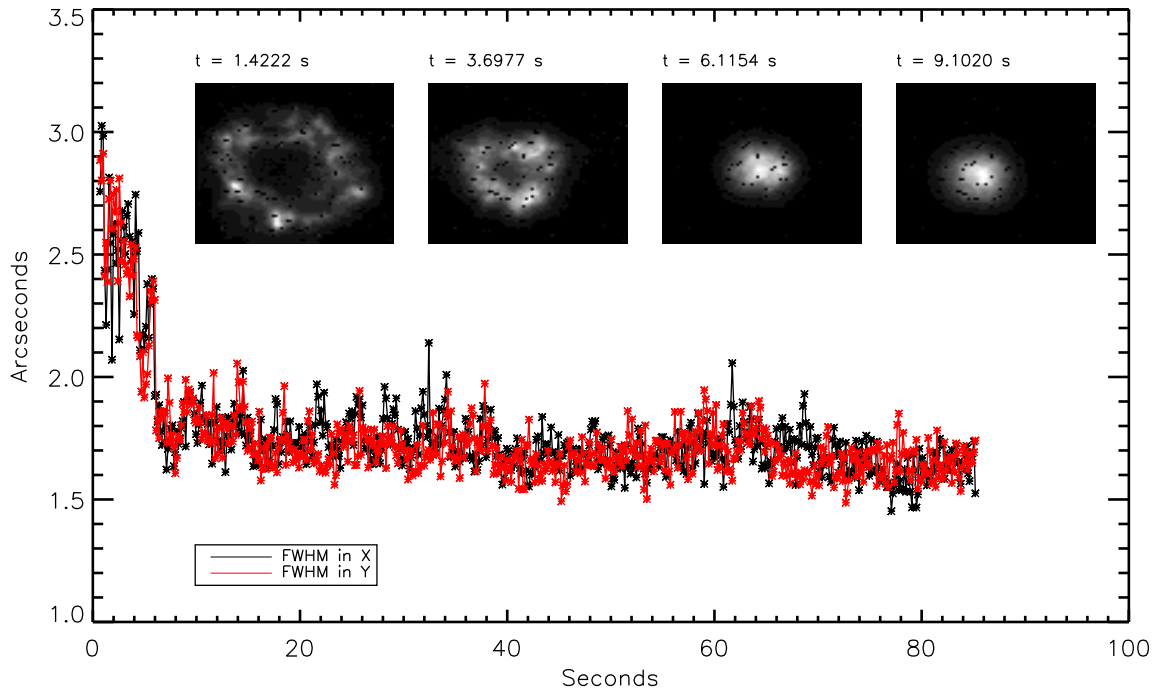


Figure 27. A plot of the full width at half maximum in the x and y directions for HD110395 as the telescope is focused. Some sample CDS frames are shown with the time at which they were imaged listed above. The black pixels are bad pixels that have been zeroed to avoid contamination.

6. WINDOW MODE-FOCUSING, IMAGE MOTION, AND TRACKING

6.1 Telescope Focusing

A very practical use of *window mode* on the H4RG is rapid imaging of a bright star for the purpose of focusing a telescope in real time. The term *real time* means that there is no delay between making an adjustment on the focus and seeing its effect on the psf as there is with many typical focusing cameras available at telescopes. Such a delay can be quite painful if the motors controlling the secondary mirror in a cassegrain configuration exhibit hysteresis.

We used *single window mode* to adjust the telescope focus before each of our *full frame* exposures. An example in which a magnitude 6 star, HD110395, was used is shown in figure 27. For this star, a 70×66 window was used so the window time was $t_w = 47.40$ ms and the cycle time was $t_c = 142.22$ ms. The CDS frames in the figure show that the time between going from an image of the telescope entrance pupil to that of a seeing-limited star is less than 10 seconds. While watching the CDS frames displayed on our graphical user interface, we were also able to get a good sense of the atmospheric conditions through the motion of the image centroid.

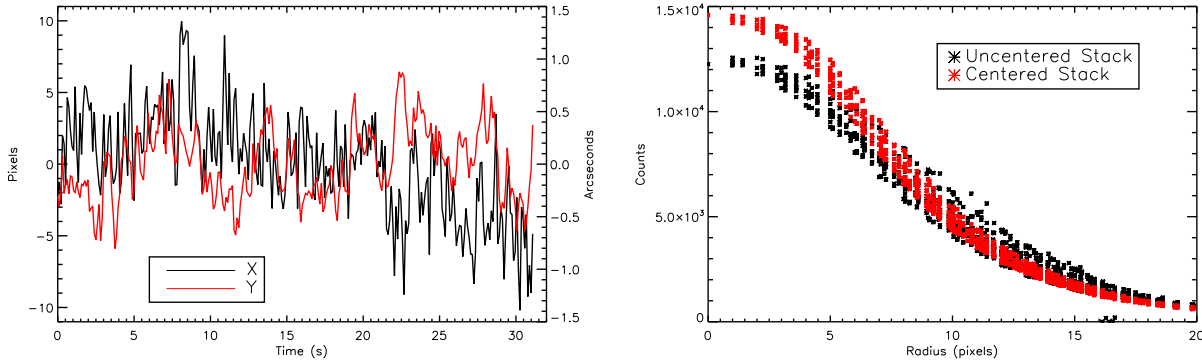


Figure 28. (Left) A plot of centroid motion vs. time for single *window mode* observations of HD103578. (Right) A comparison of radial plots for a 30×30 section of stacked images of the star. The centered image was shifted to account for centroid motion; the uncentered one was not.

6.2 Image Centroid Motion

It is well known that atmospheric turbulence causes, among other things, random motion of diffraction-limited images formed by telescopes. Windshake of a telescope and jittering in its tracking motors can also produce a similar effect. The effect is especially pronounced for short exposure times ($\sim 10^{-3}$ s) such as the ones we used in *window mode*. While watching the CDS frames displayed on the graphical user interface, we could see the stellar image "bounce around" the detector from frame to frame. For long exposures, this image motion has the effect of a low-pass filter and results in a slight blurring of the PSF.

Adaptive optics systems seek to correct this motion by applying fast corrections to the telescope optics. In particular, x, y translation of the focal plane can be used to compensate for image centroid motion and its low pass filtering effect, resulting in a more resolved image. With our closely spaced *window mode* images of stars we can produce a similar effect in software by shifting each image by x and y pixels so that their centroids line up, and then stack them by summing them or taking the mean. This shifted stacked image can then be compared to a stacked image in which the centroids were not lined up in order to gauge the amount of PSF degradation due to the image motion.

Figure 28 shows a comparison between shifted and unshifted stacks of 300 CDS images of the magnitude 5.5 star HD103578 taken through the i band filter. The window used on the star was 55×61 pixels, yielding a window time of $t_w = 34.7$ ms and a cycle time of $t_c = 104$ ms. Even though the star is saturated and flattened near the peak, the blurring effect is apparent. The FWHM of the shifted stack is 8.2 pixels while that of the unshifted stack is 9.6 pixels. The motion of the centroids is also plotted in the figure. Their standard deviations are $\sigma_x = 3.575$ and $\sigma_y = 2.478$. The larger value in x appears to be a result of a net drift in the image motion over time, likely due to tracking errors rather than the wind or any other high frequency effect.

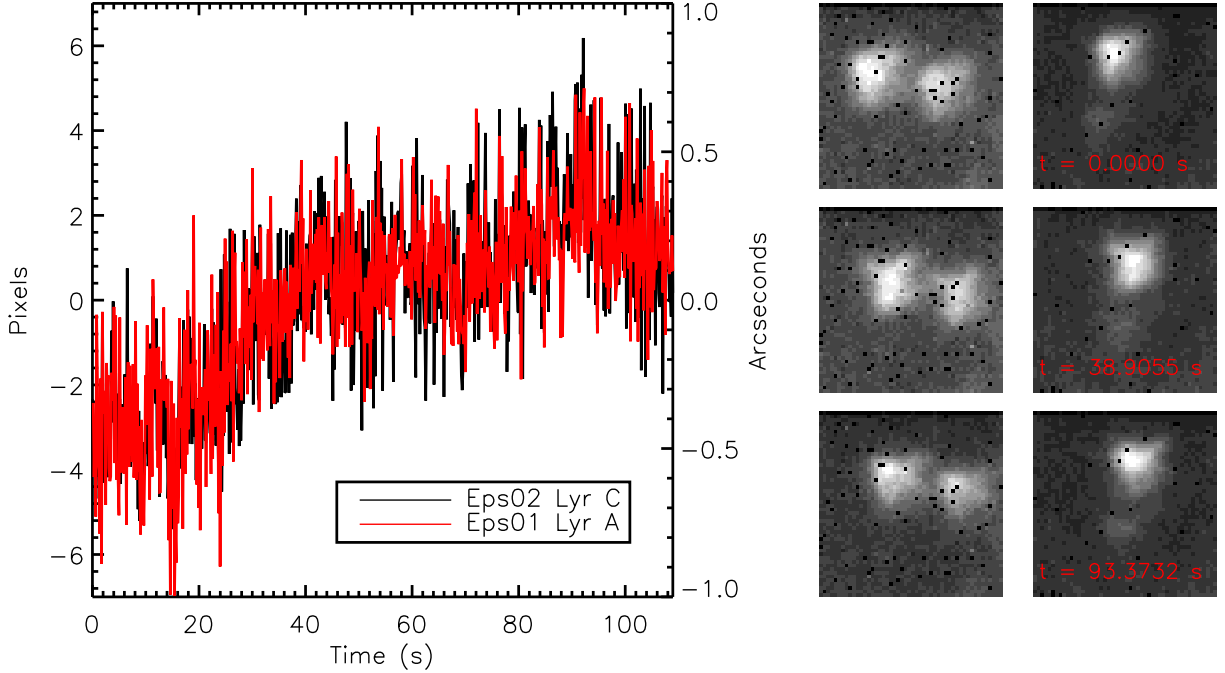


Figure 29. (Left) A plot of the x coordinate of centroid motion vs. time for multiple window images of two stars in Epsilon Lyra. (Right) Unshifted stacks of 50 consecutive CDS images of the stars. The time of the first read in the stack is listed.

6.3 Tracking with multiple windows

One of the possible uses of *multiple window* mode on the H4RG is tracking stars for telescope guiding. Using multiple guide stars across the field of view of the telescope makes it possible to detect tracking errors in the form of both uniform translation and rotation of the field. With only one guide star it is difficult to make a distinction between these two motions on short timescales. The H4RG is also capable of operating in a *guide mode* in which windows are used to image the guide stars at a fast rate while the rest of the detector is integrating. We did not have a chance to implement this *guide mode* but hope to do so in future observations.

To test *multiple window* mode for tracking, we observed several systems known to contain multiple bright stars within an $8' \times 8'$ field. One of these was Epsilon Lyra, also known as the “Double Double”. This system contains two sets of closely spaced ($< 4''$) double stars separated by $3.36'$. The first set containing Eps01 Lyr A ($M_V=5.06$) and Eps01 Lyr B ($M_V=6.1$) is the vertically separated pair on the right in Figure 29 and the second set containing Eps02 Lyr C ($M_V= 5.14$) and Eps02 Lyr D ($M_V=5.37$) is the horizontally separated pair on the left in the figure. Each binary pair was observed with a 50×50 window, giving a window time of $t_w = 25.9$ ms, an exposure time of $t_e = 51.8$ ms, and a cycle time of $t_c^{mw} = 155.6$ ms. The coordinates for the windows, $(X_{start}, X_{stop}, Y_{start}, Y_{stop})$, were $(1717, 1767, 2126, 2176)$ for the Eps02 stars and $(1473, 1523, 485, 535)$ for the Eps01 stars.

Figure 29 also shows the x centroid for one of the stars in each pair vs. time. It is clear from that the plot the stars are slowly drifting to the right in the frames and this is also evident in the stacks of 50 unshifted images. The y centroid does not show a drift over the same time interval. As mentioned in 3, the telescope was not using a guider. Since the Eps 02 pair is imaged near the center of the detector and the Eps 01 pair is imaged near the bottom part of the detector, the uniform motion in the x direction suggests that the drift is a result of error in the telescope drives rather than the rotator. Such information could have been fed back to the telescope control system to correct the errors.

It should be mentioned that t_w , t_{mw} , and t_e in this particular example are by no means optimized. In fact, these stars are of sufficient brightness that the pixel time, t_p , could be changed to $\sim 6\mu s$ and the window size could be made smaller (in order to increase the sampling rate) while still maintaining an acceptable signal to noise ratio for the purposes of guiding. The 200 Hz sampling rate required by some guiding systems should be possible with the H4RG with the proper choice of guide stars.

APPENDIX A. S/N

For a given source magnitude M_s and a background flux B , we can calculate the Signal to Noise Ratio (SNR) as

$$\frac{S}{N} = \frac{I_o A t * 10^{-(M-M_o)/2.5}}{\sqrt{Bt} + I_o A t * 10^{-(M-M_o)/2.5}}, \quad (11)$$

where M_o is a magnitude of zero that corresponds to a 10^6 photons/sec/cm²/band and A is the area of the telescope in m^2 .

To obtain a signal to noise of S , then, we should expose for a time t given by

$$t = \frac{S^2(B + I_o A 10^{-(M-M_o)/2.5})}{I_o^2 A^2 10^{-2(M-M_o)/2.5}}, \quad (12)$$

APPENDIX B. IRAF PARAMETERS

The parameters used in **DAOFIND** are chosen according to the recipe laid out in Davis.¹⁷ In particular, for a given sky value, s in ADU, number of photons per ADU, p , and read noise, r , the expected 1σ variance in the sky will be

$$(\sqrt{s \times p + r^2})/p \quad (13)$$

For our images, with $s = 2.5$, $p = 1$, and $r = 0.3$ for the combinations of dithers, we have $1\sigma = \sqrt{2.5 \times 1 + 0.3^2} = 1.609$.

Most of the parameters were kept at default. We adjusted **fwhmpsf** according to the seeing for each night. It was typically between 11 pixels and 14 pixels (larger in g than in i and y), corresponding to the 1.375-1.75 arcsecond seeing at the site. Following Davis,¹⁷ we set **psfrad** = $4.5 * \text{fwhmpsf}$ and **fitrad** = **fwhmpsf**. We also adjusted **sigma** according to the number of dithers used to form the final image and the gain of the preamplifiers.

The parameter to which the finding algorithm was most sensitive was **threshold**. Several "eyeball" tests for each image were performed to determine a reasonable value for **threshold**. Fortunately, doing a few iterations of detection, psf fitting, and subtraction eliminated the need to find a perfect value for this parameter.

ACKNOWLEDGMENTS

The lab testing was performed in the Rochester Imaging Detector Laboratory with support from the NYSTAR Faculty Development Program. This work was funded, in part, by NSF grant AST-0441069, "Applying Detector Advances to the LSST Camera." We thank Buell Jannuzi, Dick Joyce, and Skip Andree of KPNO for assistance in the observing run. We thank Yibin Bai, Markus Loose, and Jim Beletic of Teledyne for their assistance in operating the detectors and the SIDECAR ASIC.

This device was obtained via private funding made available through LSST Corp. as part of the LSST sensor development program.

Funding for the SDSS and SDSS-II has been provided by the Alfred P. Sloan Foundation, the Participating Institutions, the National Science Foundation, the U.S. Department of Energy, the National Aeronautics and Space Administration, the Japanese Monbukagakusho, the Max Planck Society, and the Higher Education Funding Council for England. The SDSS Web Site is <http://www.sdss.org/>.

The SDSS is managed by the Astrophysical Research Consortium for the Participating Institutions. The Participating Institutions are the American Museum of Natural History, Astrophysical Institute Potsdam, University of Basel, University of Cambridge, Case Western Reserve University, University of Chicago, Drexel University, Fermilab, the Institute for Advanced Study, the Japan Participation Group, Johns Hopkins University, the Joint Institute for Nuclear Astrophysics, the Kavli Institute for Particle Astrophysics and Cosmology, the Korean Scientist Group, the Chinese Academy of Sciences (LAMOST), Los Alamos National Laboratory, the Max-Planck-Institute for Astronomy (MPIA), the Max-Planck-Institute for Astrophysics (MPA), New Mexico State University, Ohio State University, University of Pittsburgh, University of Portsmouth, Princeton University, the United States Naval Observatory, and the University of Washington.

REFERENCES

1. Y. Bai, S.G. Bernd, J.R. Hosack, M.C. Farriss, J.T. Montroy and J. Bajaj, "Hybrid CMOS focal plane array with extended UV and NIR response for space applications," *SPIE Proc.* **48**, 2003.
2. P. Magnan, "Detection of visible photons in CCD and CMOS: A comparative view," *Nuc. Inst. and Meth.* **504**, pp. 199–212, 2003.
3. D. Groom, "Cosmic rays and other nonsense in astronomical CCD imagers," *Exp. Astronomy* **14**(1), 2002.
4. D.F. Figer, B.J. Rauscher, M.W. Regan, E. Morse, J. Balleza, L. Bergeron and H.S. Stockman, "Demonstration of an algorithm for read-noise reduction in infrared arrays," *SPIE* **5167**(270), 2004.
5. D.F. Figer, M. Agronin, J. Balleza, R. Barkhouser, L. Bergeron, G.R. Greene, S.R. McCandliss, B.J. Rauscher, T. Reeves, M.W. Regan, U. Sharma and H.S. Stockman, "Independent testing of JWST detector prototypes," *SPIE* **4850**(981), 2003.
6. A.M. Fowler and I. Gatley, "Demonstration of an algorithm for read-noise reduction in infrared arrays," *ApJ* **353**(33), 1990.
7. B.J. Rausher, O. Fox, P. Ferruit, R.J. Hill, A. Waczynski, Y. Wen, W. Xia-Serafino, B. Mott, D. Alexander, C.K. Brambora, R. Derro, C. Engler, M. B. Garrison, T. Johnson, S.S. Manthripragada, J.M. Marsh, C. Marshall, R.J. Martineau, K.B. Shakoorzadeh, D. Wilson, W.D. Roher, M. Smith, C. Cabelli, J. Garnett, M. Loose, S. Wong-Anglin, M. Zandian, E. Cheng, T. Ellis, B. Howe, M. Jurado, G. Lee, J. Nieznanski, P. Wallis, J. York, M.W. Regan, D.N.B. Hall, K. W. Hodapp, T. Böoker, G.D. Marchi, P. Jakobsen and P. Strada, "Detectors for the James Webb Space Telescope Near-Infrared Spectrograph I: Readout mode, noise model, and calibration considerations," *arXiv:0706.2344v1*, 15 Jun 2007.
8. William H. Press, William T. Vetterling, Saul A. Teukolsky and Brian P. Flannery, *Numerical Recipes in C: The Art of Scientific Computing*, Cambridge University Press, New York, NY, 1992.
9. H. Bushouse, C. Skinner and J. MacKenty, "The STScI NICMOS pipeline: CALNICA, single image reduction," June 10, 1996.
10. G. Verdoes, R. Vermeij, E. Valentijn and K. Kuijken, "The secondary standards program for OmegaCAM at the VST," *arXiv:astro-ph/0612469v1*, 18 Dec 2006.
11. P. Stetson, "Some factors affecting the accuracy of stellar photometry with CCDs," *DAO Preprint*, September 1988.
12. S. Jester, et al, "The Sloan Digital Sky Survey view of the Palomar-Green bright quasar survey," *ApJ* **130**, pp. 873–895, 2005.
13. A.U. Landolt, "UBV photoelectric sequences in the celestial equatorial selected areas 92-115," *AJ* **78**(959), 1973.
14. A.U. Landolt, "UBVRI photometric standard stars in the magnitude range $11.5 < V < 16.0$ around the celestial equator," *ApJ* **104**(1), 1992.
15. C.A. Gullixson, P.C. Boeshaar, J.A. Tyson, and P. Seitzer, "The B_jRI photometric system," *ApJS* **99**, pp. 281–993, 1995.
16. L.A. Hillenbrand, J.B. Foster, S.E. Persson and K. Matthews, "The Y band at 1.035 microns: Photometric calibration and the dwarf stellar/substellar color sequence," *PASP* **114**, pp. 708–720, 2002.
17. P. Massey, Lindsay E. Davis, *A User's Guid to Stellar CCD Photometry with IRAF*, 1992.